INSTITUT DE FRANCE
Académie des sciences

Comptes Rendus

Mécanique

Yuan-Chao Zhang, Yu-Jing Jiang, Xiao-Jie Tang, Miao Chen and Xin-Shuai Shi

Cracking behavior and local stress characteristics around the opening surrounded by two intermittent joints: experiment and numerical simulation

Volume 348, issue 1 (2020), p. 33-61

Published online: 30 March 2020

https://doi.org/10.5802/crmeca.4

Les Comptes Rendus. Mécanique *sont membres du Centre Mersenne pour l'édition scientifique ouverte*
www.centre-mersenne.org
e-ISSN : 1873-7234

Comptes Rendus
Mécanique
2020, 348, nº 1, p. 33-61
https://doi.org/10.5802/crmeca.4

Rupture / *Rupture*

Cracking behavior and local stress characteristics around the opening surrounded by two intermittent joints: experiment and numerical simulation

Yuan-Chao Zhang [a], Yu-Jing Jiang [*, a], Xiao-Jie Tang [b], Miao Chen [c, d] and Xin-Shuai Shi [d]

[a] Graduate School of Engineering, Nagasaki University, Nagasaki 8528521, Japan

[b] Department of Civil Engineering, The University of Hong kong, Hong kong, PR China

[c] College of Mining and Safety Engineering, Shandong University of Science and Technology, Qingdao 266590, PR China

[d] State Key Laboratory for Geomechanics and Deep Underground Engineering, China University of Mining and Technology, Xuzhou 221116, PR China.

E-mails: zhangyc4418@163.com (Y.-C. Zhang), jiang@nagasaki-u.ac.jp (Y.-J. Jiang), tangxiaojie_edu@163.com (X.-J. Tang), miaochen@cumt.edu.cn (M. Chen), xs_shi@cumt.edu.cn (X.-S. Shi).

Abstract. In this research, the Strength and deformation behaviors, cracking process, and local stress evolution of sandstone specimens containing a circular opening and two joints (called H-J sandstone specimens in this study) were researched by experiment and numerical simulation (two-dimension particle flow code). The effect of different joint positions around the opening has been specifically studied by changing the ligament angle (β). The test results show that peak strength and peak strain firstly decrease then increase with the increasing β, while the peak strain presents an overall upward trend. Three types of coalescence failure patterns between the opening and joints formed, and the corresponding cracking process and acoustic emission (AE) characteristics are highly related to the ligament angle. Based on the micro-parameters calibration, a good agreement was achieved between experimental and numerical simulation. The numerical results show that the local stress evolution around the opening is highly corresponding to the cracking process. The microcracks initiation and propagation cause obvious stress fluctuations, drops or increasements of minimum principal stress, while the cracks coalescence results in obvious reduction of maximum principal stress and drops of stress-strain curve. It also be found that the stress distribution and magnitude around the opening tend to be closely related to both coalescence failure and strength characteristics of H-J specimens. Finally, the cracking mechanism between the opening and joints was revealed based on particle displacement fields. The results show that different cracking mechanism may cause different local stress changes, which finally determines the overall mechanical behavior of specimens.

Keywords. Sandstone, Opening, Joints, Cracking, Stress evolution, Particle flow code.

Manuscript received 19th June 2019, revised 23rd August 2019, accepted 19th November 2019.

1. Introduction

With the growing demand for energy and space in human society, the underground engineering has developed rapidly in recent decades, e.g. tunnel, mining, geothermal extraction and CO2 geological sequestration etc. However, complex geological rock mass poses great challenges to underground constructions for its discontinuity, inhomogeneity and anisotropy, mostly caused by the existence of flaws, joints, cracks, and faults, etc [1]. Generally, the stress disturbance caused by the underground excavation in the jointed rock mass will cause tensile or compressive stress concentration around the opening and flaws, resulting in the cracks initiation, propagation and eventually coalescence failure of surrounding rock mass. Therefore, the failure behavior and stress interaction between the opening and adjacent joints should be further understood.

Most joints or flaws are non-persistently existed in the rock mass [2]. The strength and stiffness of rock mass are greatly influenced by the geometric and mechanical properties of the non-persistent joints. Therefore, the strength, deformation and cracking process of pre-cracked rock or rock-like specimens have been widely investigated based on the dip angle of single joint [3, 4], parallelity [5, 6] or non-parallelity [7, 8] or coplanarity [9, 10] of two joints, and even the dip, space, continuity of joint sets [11, 12], etc. It can be concluded that the wing cracks, anti-wing cracks and secondary cracks usually initiate from the joint tips, and different coalescence modes (tension, shear, or mixed tension and shear) may form with different relative positions of joints, indicating different interaction mechanisms between the joints. However, it is more complex when the opening is excavated in the jointed rock mass for the interaction between the the opening and surrounding joints, which may result in more unconventional and complex failure around the opening. In general, the failure of opening mainly located on the top and sides, such as the roof fall and rib spalling of tunnel or roadway [13, 14]. However, when a fault or weak plane is encountered, the deformation and plastic region size of opening tend to become larger, for the activation or shear deformation of fault or weak plane [15, 16, 17]. In order to further explore the failure characteristics and mechanisms of the excavated opening in jointed rock mass, many simplified small-scale physical tests were conducted under the uniaxial and biaxial compression. Sagong *et al.* [18] observed the interactive tensile cracks generation and removable block formation between the opening and joints by changing the joint angles. The rock specimen containing two square openings and one pre-existing fissure [19], specimens containing combined flaws [20] and SHWF/THWF specimens [21] were carried out the experiments or numerical simulations. Their results proved that the strength and deformation characteristics, crack coalescence patterns, stress distribution around the opening are all highly dependent to the joint angle. It further be found that failure intensity of the opening was also related to the frictional coefficients of structural planes [22] and confining pressure level [23].

Recent years, numerical simulation methods have been widely used in rock mechanics and rock engineerings. Various numerical simulation methods are applied to investigate the failure behavior of brittle materials, including the finite element method [24, 25], the boundary element method [26, 27], the rock fracture process analysis [28, 29, 30], the distinct element method [31, 32, 33, 34, 35, 36], the discontinuous deformation analysis [37], and some other methods such as extended finite element method [38] and the combined finite/discrete method [22], etc. Among these numerical methods, particle flow code (PFC) tends to be more popular to simulate the crack initiation, propagation and coalescence behavior and reveal the micro-level mechanical mechanism of rock or rock-like specimens containing hole and/or flaws. For example, the cracking process of rock-like specimens containing single flaw [39, 40], two flaws [8, 41] and

* Corresponding author.

multiple non-persistent joints [42, 43] were investigated by using PFC. Yang *et al.* [44] used PFC to explore the failure behavior of the circular opening in non-persistently jointed rock mass and observed three failure patterns, i.e. step path failure, planar failure and rotation failure. Yang *et al.* [45] further found that the coalescence modes between the opening and adjacent joints are classified into three modes, i.e. tension coalescence, shear coalescence and removable block coalescence, which are closely related to the dip angle of joints.

Although lots of experimental and numerical investigations have been conducted to explore the failure behavior of opening in jointed rock mass, the main focus are placed on the inclination or number of the joints. The relative position between the opening and surrounding joints is rarely considered. The coalescence failure patterns, stress distribution and evolution around the opening should be further researched with the consideration of different joints positions. In the present study, two open joints and a circular opening are prefabricated in the sandstone specimens. Different relative locations are achieved by changing the rock bridge angle (i.e. ligament angle). Uniaxial compressive tests are firstly conducted combined by acoustic emission system and high definition camera. Later, Based on the test results, PFC models are constructed and calibrated. Therefore, the strength, deformation and cracking behavior can be revealed by test results, while the stress distribution and evolution, as well as cracking mechanism, can be revealed by numerical results. This research is greatly significant for understanding the stability of excavated opening in jointed rock mass.

2. Experimental material and testing procedure

2.1. *Sandstone material*

Sandstone has been widely used to study rock mechanics problems, especially for studying the strength, deformation and failure characteristics of rock specimens. This is mainly because sandstone is main underground engineering rock mass, easy to sample, and particularly homogeneous. In this research, sandstone materials are chosen from Ju'nan City, Shandong Province of China. This sandstone has a medium-grained structure with an average unit weight of 23.9 kN/m^3.

2.2. *Preparation of specimens containing the opening and joints*

In this research, all of these rectangular sandstone specimens were cut from the same rock block to minimize the effects of mechanical anisotropy. Based on the previous studies [4, 7, 8], the ratio of height to width of tested specimens is set to 2.0 in order to minimize the effect of end friction on the testing results. Therefore, all these specimens were designed to be 130 mm in height, 65 mm in width and 25 mm in thickness.

The sandstone specimens were pre-flawed by a circular opening and two open joints around the opening, which are called H-J sandstone specimens in this study. The geometry of flaws in sandstone specimens is defined by five parameters: the joint angle (α); the joint length (L_j); the ligament angle (β); the ligament length (L_r); the opening diameter (d), as shown in Figure 1. In this study, different geometric locations of joints around the opening were achieved by varying the ligament angle ($\beta = 0°\sim90°$), while keeping the other parameters constant ($\alpha = 45°$, $L_\mathrm{j} =$ 10 mm, $L_\mathrm{r} = 30$ mm, $d = 15$ mm). A detailed description of the sandstone specimens with different flaw geometries is listed in Table 1. Intact specimens and single-holed specimens were also prepared for comparison. Note that the tested sample size and geometric parameters of circular opening and joints are determined mainly considering the main variable (i.e. ligament angle, $\beta = 0°\sim90°$) and the feasibility of the current testing conditions (such as the loading capacity and loading space).

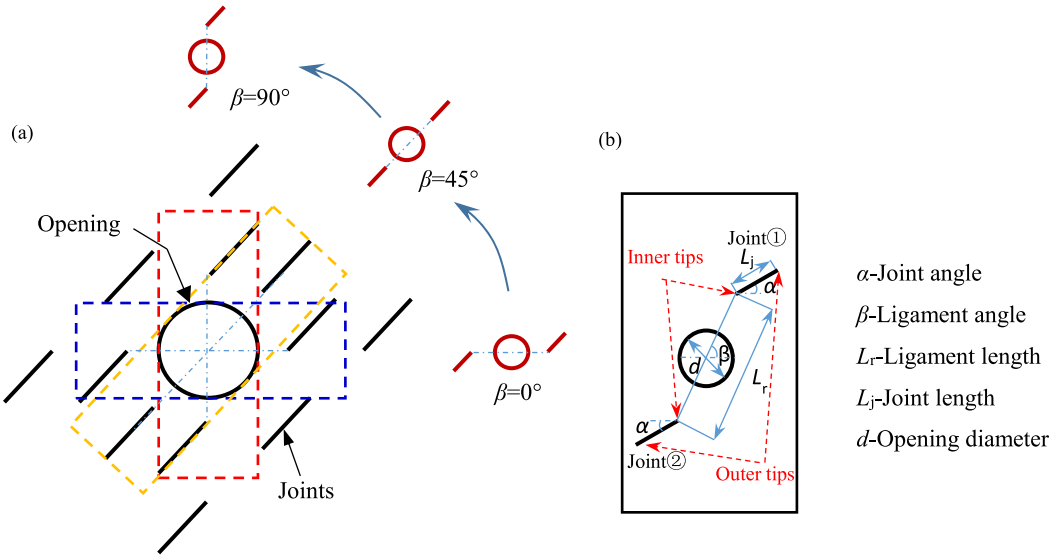

Figure 1. The relative position between the opening and surrounded non-persistent joints (a) and simplified research model in this study (b).

Table 1. Tested sandstone specimens containing a circular opening and two open joints

Specimens	W/mm	H/mm	T/mm	α/°	β/°	L_j/mm	L_r/mm	d/mm
WZ-1	65.53	130.19	25.05			Intact specimen		
WZ-3	65.50	130.26	26.10			Intact specimen		
SH-1	65.82	130.31	25.95			Single-hole specimen		
SH-2	65.88	130.39	25.26			Single-hole specimen		
S0-2	65.52	130.23	25.22	45	0	10	30	15
S0-3	66.58	130.50	25.46	45	0	10	30	15
S15-1	65.00	130.29	25.25	45	15	10	30	15
S15-2	65.76	129.52	26.10	45	15	10	30	15
S30-2	65.58	130.06	26.01	45	30	10	30	15
S30-3	65.64	130.17	25.17	45	30	10	30	15
S45-1	65.65	130.26	25.11	45	45	10	30	15
S45-2	66.07	130.52	26.12	45	45	10	30	15
S60-1	65.10	130.01	25.10	45	60	10	30	15
S60-2	66.35	130.26	25.49	45	60	10	30	15
S75-2	65.53	129.92	25.60	45	75	10	30	15
S75-3	65.28	130.28	25.73	45	75	10	30	15
S90-1	65.50	130.21	25.80	45	90	10	30	15
S90-3	66.32	130.30	25.08	45	90	10	30	15

Note: W-Width; H-Height; T-Thickness.

2.3. *Testing system and testing procedure*

All sandstone specimens were subjected to uniaxial compression tests using MTS servo-controlled testing system with a maximum axial force of 300 kN, as shown in Figure 2(a). The axial stress (i.e. σ_1) acts on the top and bottom surfaces of specimen through two smooth

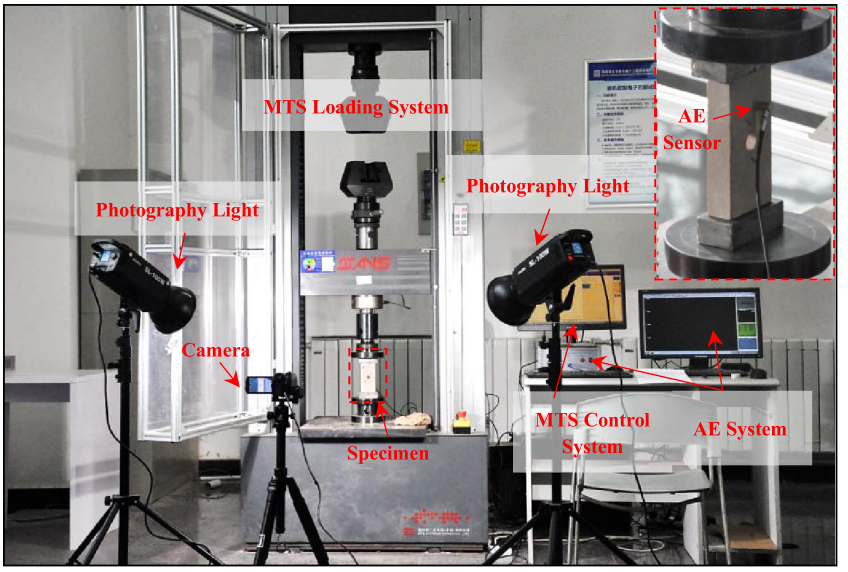

(a) Testing system

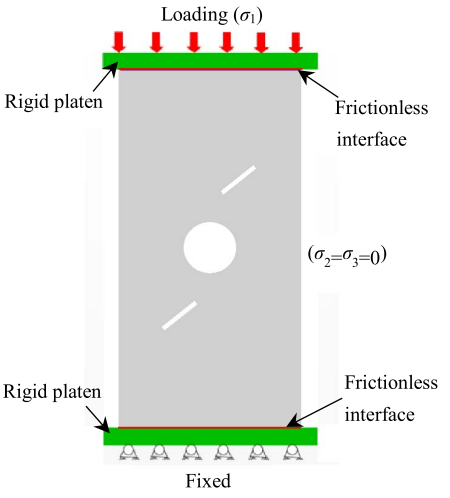

(b) Boundary conditions

Figure 2. (a) Testing system and (b) boundary conditions of specimens in this research.

rigid steel blocks until the specimen failure took place, while all the other sides are free faces (i.e. $\sigma_2 = \sigma_3 = 0$), as shown in Figure 2(b). The tests were conducted under the condition of displacement-control with 0.12 mm/min (about a strain rate of 1.5×10^{-6}/s), which ensures a quasi-static loading process.

The failure process of specimen was captured with a digital camera assisted by two photography lights for recording a clearer crack propagation process. In addition, to investigate the fracture coalescence characteristics of deforming specimens during testing, the acoustic emission (AE) system was adopted. The AE counts were recorded by an AE measuring system. The frequency of the AE system was set to 3 MHz. AE sensor was attached to the back face of sandstone specimen using a hot bar as a coupling agent to collect and transmit AE signals.

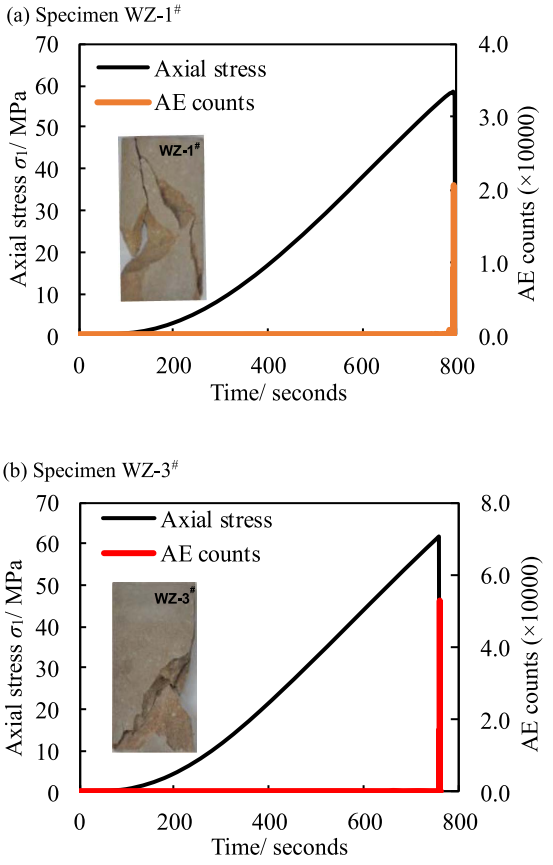

Figure 3. Experimental results of intact sandstone specimens under uniaxial compression. (a) Specimen WZ-1$^{\#}$. (b) Specimen WZ-3$^{\#}$.

3. Experimental results

3.1. *Strength and deformation behavior of H-J sandstone specimens*

The axial stress-time curves and ultimate failure modes of two intact sandstone specimens are shown in Figure 3. We can conclude that the tested sandstone is obviously brittle, any cracks propagation, coalescence and AE events were not observed prior to the peak stress. The specimen failed abruptly in a few seconds after peak stress with a strong sound, which was also testified by an intense AE event. The strength and deformation properties of the two intact sandstone specimens have a good consistency, while the failure modes of specimen WZ-1$^{\#}$ (splitting type) and WZ-3$^{\#}$ (shear type) are different. The difference of failure modes of two intact specimens may be caused by the mineralogy, shape, size and size distribution. Therefore, we repeated the tests twice for each ligament angle (β) to obtain the best test results.

Figure 4 shows the axial stress-strain curves of H-J sandstone specimens under uniaxial compression. Generally, the effect of specimen variability on the mechanical parameters such as uniaxial compressive strength and elastic modulus is very small. The observed slight difference of stress-strain curves for the same ligament angle is mainly due to difference of unstable failure process near or after the peak stress.

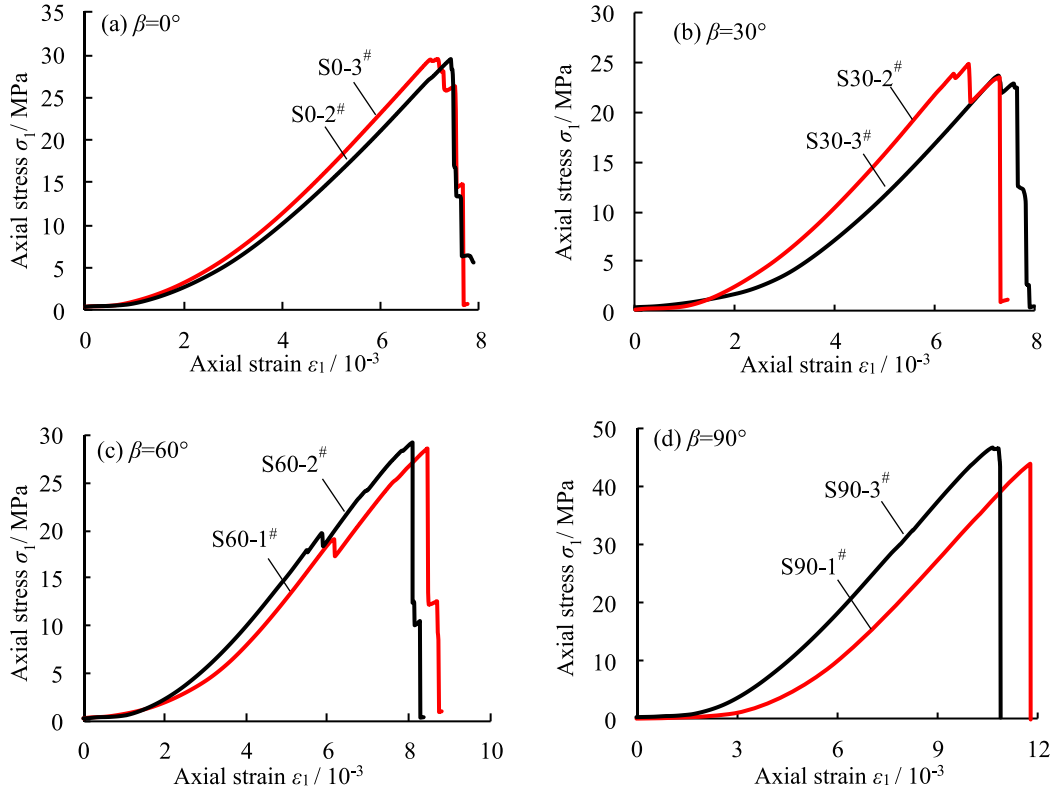

Figure 4. Effect of specimen variability on stress-strain curves of H-J sandstone specimens.

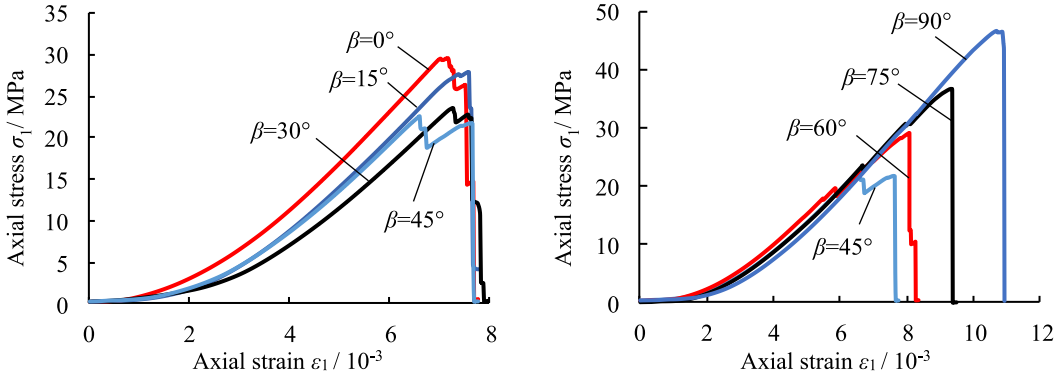

Figure 5. Effect of ligament angle on stress-strain curves of H-J sandstone specimens.

Figure 5 shows the stress-strain curves of H-J specimens with different ligament angle ($\beta = 0°$~$90°$). In general, these H-J specimens show an initial nonlinear deformation caused by closure of primary fissures or pores in rock material. Subsequently, elastic deformation begins to dominate the axial stress-strain curve, and the axial stress has an approximately linear relation with the axial strain. Obvious stress drops can be observed near the peak stress due to the crack coalescence in the specimen. It can be found that the stress fluctuations near the peak stress is more obvious when $\beta = 0°$~$45°$ than that of $\beta = 60°$~$90°$, which reflects the different rupture

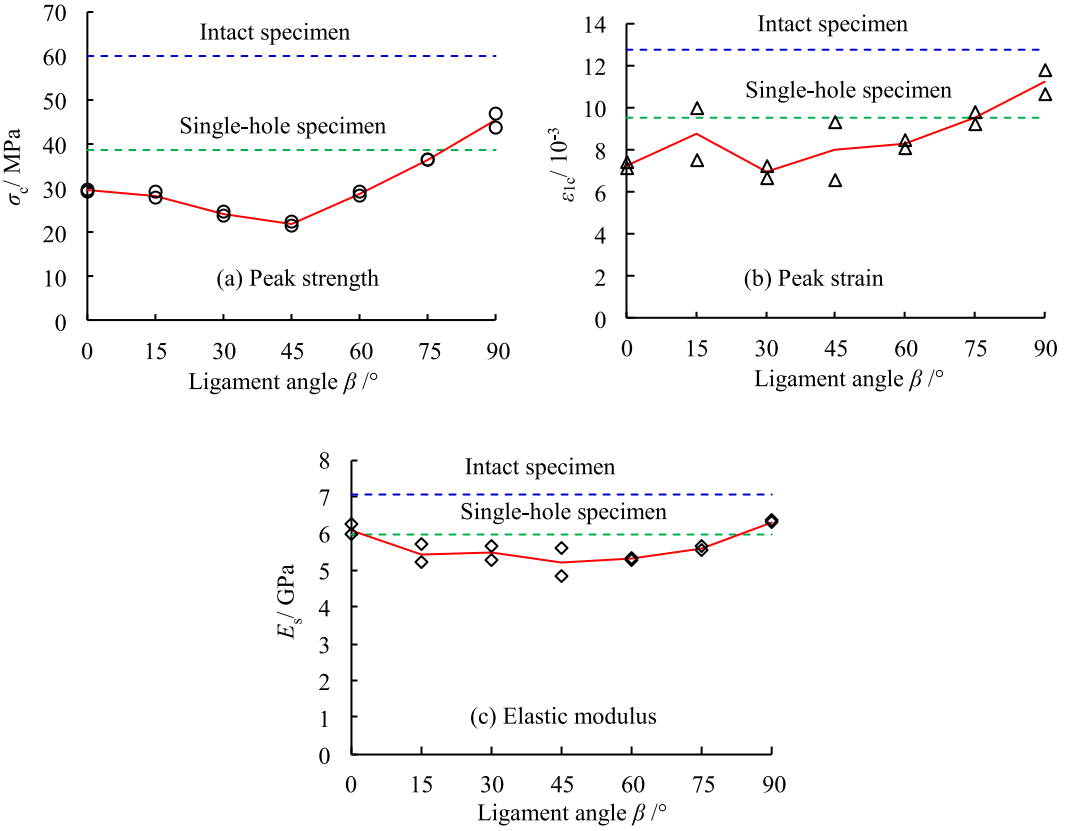

Figure 6. Influence of ligament angle on strength and deformation parameters of H-J sandstone specimens. (a) Peak strength. (b) Peak strain. (c) Elastic modulus.

evolution process of specimens with different ligament angle. However, all these H-J specimens failed finally in a brittle unstable manner with the increase of axial strain.

Figure 6 depicts the influence of ligament angle on the strength and deformation parameters of H-J sandstone specimens, which were also compared with the intact and single-hole specimens. In Figure 6, σ_c and ε_{1c} are the peak strength (i.e. uniaxial compressive strength, UCS) and peak axial strain of specimens, respectively, and E_s is the elastic modulus, i.e. the average slope in the linear elastic range of stress-strain curve. The following analysis is based on the average values of two specimens for the same ligament angle.

Figure 6(a) shows the relationship between peak strength and ligament angle. we can conclude that the peak strength of H-J sandstone specimen firstly decreases (29.52 MPa→22.03 MPa, a 25.37% reduction) when β increase from 0° to 45° and then increases (22.03→45.38 MPa, a 105.99% growth) when β increase from 45° to 90°. The minimum strength value is reached at β = 45°. Figure 6(b) shows that peak strain, overall, takes on an upward trend, except for the case of β = 15°. It can be seen from Figure 6(c) that the variation of elastic modulus with the increasing ligament angle is similar to that of peak strength, but the magnitude of change is much smaller: when β increase from 0° to 45°, the elastic modulus drops from 6.11 GPa to 5.21 GPa, a 14.73% reduction; when β increase from 45° to 90°, the elastic modulus increases from 5.21 GPa to 6.33 GPa, a 21.49% growth.

From Figure 6(a)~(c), it can be found that: compared with the intact and single-hole specimens, the strength and deformation parameters of H-J specimens with various ligament angle

are all lower than the intact sandstone specimens. However, the peak strength, peak strain and elastic modulus of H-J specimens with ligament angle of 75° and 90° are close to or even higher than that of single-hole specimen, although they are lower at the case of $\beta = 0°\sim60°$. The above means that the existence of opening and joints obviously reduces the strength and stiffness of rock mass and the reduction degree is related to the ligament angle. It seems that the underground opening excavated in jointed rock mass with a higher ligament angle (75°~90°) is more safer than with a lower ligament angle, especially for $\beta = 45°$.

3.2. *Cracking process and AE behavior of H-J sandstone specimens*

Figure 7 shows the ultimate failure modes of H-J specimens under uniaxial compression, for comparision, the failure modes of single-hole specimens are also given. It can be found that the failure modes of specimens with the same flaw geometry are very similar, except for some minor differences. This indicates the heterogeneity of sandstone materials has a very small effect on the failure characteristics in this research. In addition, the failure modes of H-J specimens are more complicated than single-hole specimens for the cracking coalescence inside or near the rock bridge area between the opening and joints.

Based on the previous studies on the cracking behavior of pre-holed or pre-cracked rock materials [4, 46, 47], several common crack types can also be identified in the failed specimens in this research, as labelled in Figure 7, including: (i) shear and tensile cracks initiated from the left and right sides of the hole; (ii) the wing crack, anti-wing crack and secondary crack initiated from the tips of the joints; (iii) far-field crack, lateral crack and surface spalling. However, the coalescence cracks directly or indirectly connecting the opening and joints in failed H-J specimens can not be easily identified as the above common crack types for their different crack characteristics. Therefore, detailed discussion about the coalescence cracks types will be done in the following section.

As can be seen from Figure 7, the failure of H-J sandstone specimens is caused by the combination of several types of craks, and the coalescence modes between the opening and its surrounding joints highly depend on the ligament angle. Three distinct coalescence modes can be summarized as follows.

Mode I: Indirect crack coalescence failure ($\beta = 0°\sim30°$). The cracks initiated from the left and right sides of opening then coalesced with the anti-wing crack (in most case) or secondary crack (in a few case such as the left coalescence of S0-3$^{\#}$). Usually, the coalescence sites are located on the upper or/and lower sides of the rock bridge area.

Mode II: Single crack coalescence failure ($\beta = 45°$ and 60°). A direct coalescence by a single crack between the opening and the inner tips of joints occurred through the rock bridge area.

Mode III: Multiple cracks coalescence failure (or Removable blocks failure, $\beta = 75°$ and 90°). Two or three coalescence cracks were formed between the opening and inner tips as well as outer tips of joints. Usually, smaller or larger removable blocks can form near the top and bottom of opening. Thus, this coalescence mode can also be called removable block coalescence failure.

To investigate the cracking process of H-J specimens, photography and acoustic emission (AE) monitoring were used in the tests. Figure 8 show the stress-time curve, AE counts, accumulated AE counts and the corresponding cracks evolution sketch of H-J sandstone specimens with different ligament angle. The numbers in these figures denote the cracking order in the specimen observed by photographic monitoring, and the superscript letters on the same numbers mean that these cracks were simultaneously initiating from different positions.

As shown in Figure 8(a)~(b). When $\beta = 0°$ and 30°, the Anti-wing cracks firstly initiate from the inner tips of joints (e.g. the cracks $1^{a\sim b}$ in S30-3$^{\#}$ and crack 1^{a} in S0-3$^{\#}$). After that, the indirect coalescence between the opening and joints occurs by the cracks $2^{a\sim b}$ in S30-3$^{\#}$ and crack 2

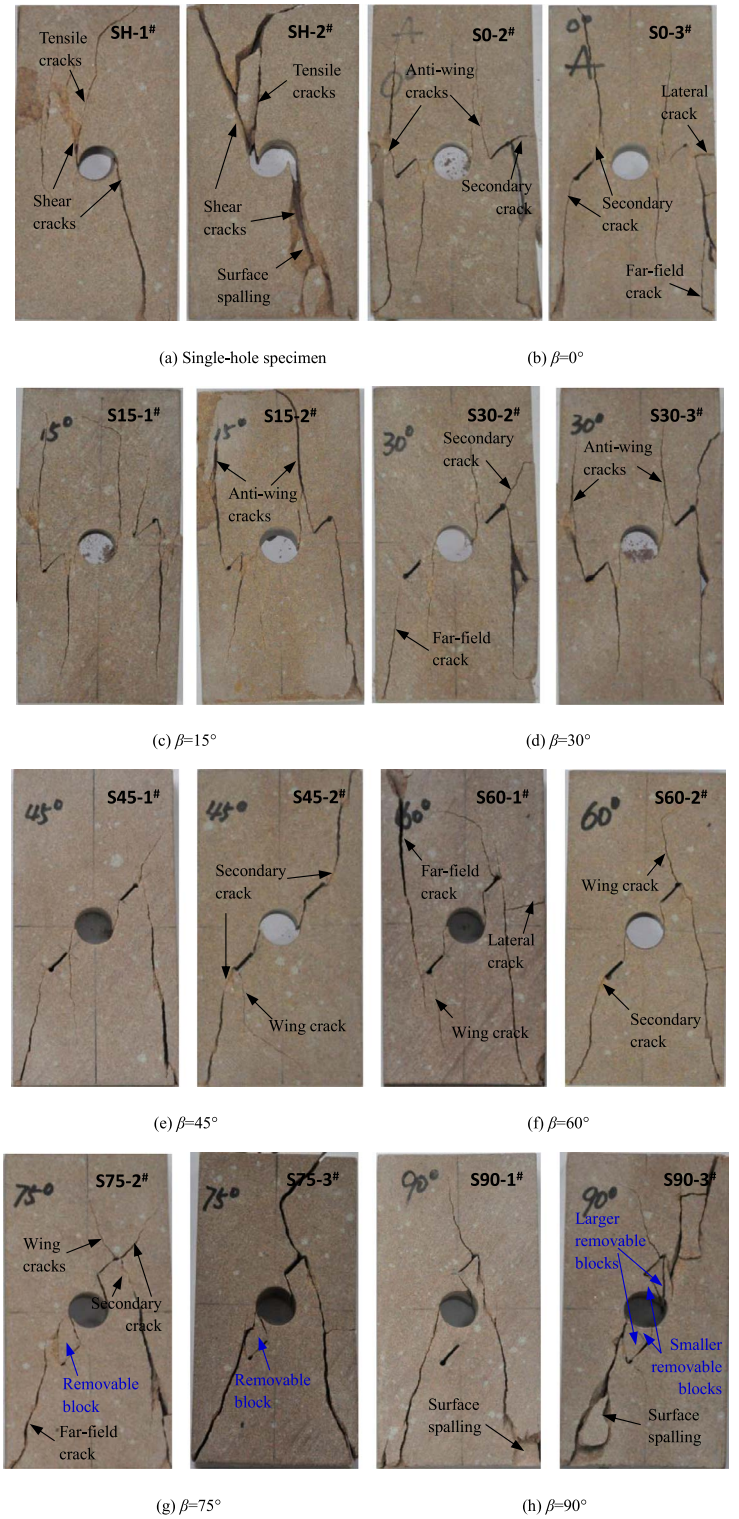

Figure 7. Ultimate failure modes of single-hole specimens and H-J specimens with different ligament angles.

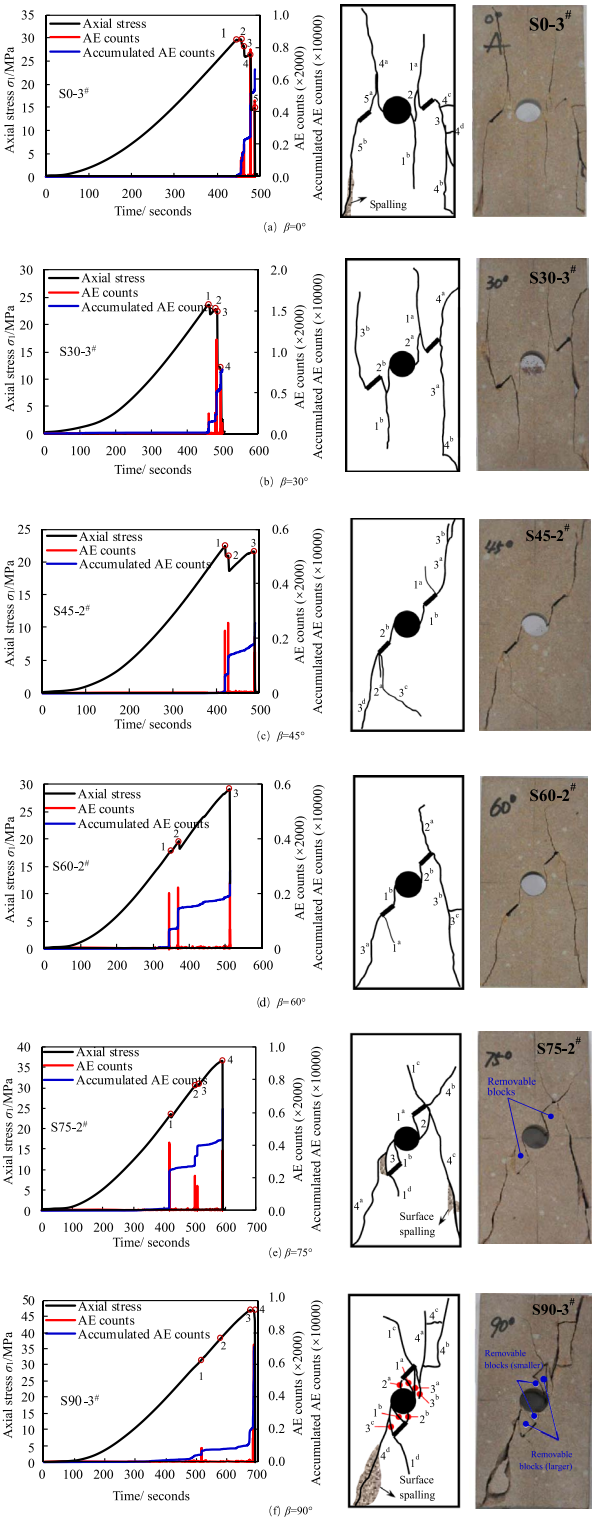

Figure 8. The axial stress, AE counts and cracking evolution sketch of H-J sandstone specimens with different ligament angle.

in S0-3$^{\#}$. The final failure is reached by the subsequent anti-wing cracks 3$^{a\sim b}$, secondary crak 4^{a} and far-field carck 4^{b} in specimen S30-3$^{\#}$. It should be noted that the failure process is more complex from 4$^{a\sim d}$ to 5$^{a\sim b}$ in S0-3$^{\#}$. This may be caused by some mechanical difference between joint ① and ② in S0-3$^{\#}$, which can be proved by the different types of cracks initiated from two joints (anti-wing crack 1^{a} and 3 initiates from joint ① while secondary cracks 5$^{a\sim b}$ initiates from joint ②). The entire rupure process of both S0-3$^{\#}$ and S30-3$^{\#}$ mainly occurs in the post-peak stage. The cracks initiation and coalescence (from point 1 to 2) cause small stress drop and weak AE events, while large stress drops and strong AE events mainly occur at points 4∼5 of S0-3$^{\#}$ and points 3∼4 of S30-3$^{\#}$, i.e. the ultimate coalescence failure between the outer joint tips and specimen boundaries.

As shown in Figure 8(c)∼(d). When $\beta = 45°$ and 60°, the initiation of wing crack at the outer tips of joints seems to be together with the coalescence crack connecting the inner tips and the opening, (e.g. the 1^{a} and 1^{b} from joint ① in specimen S45-2$^{\#}$ and the 1^{a} and 1^{b} from joint ② in specimen S60-2$^{\#}$). The coalescence between the opening and two joints (① and ②) does not occur simultaneously, but for a short time. The final failure of specimen was mainly caused by the extension of secondary carcks initiated from the outer joint tips (e.g. 3^{a}, 3^{b}, 3^{d} in S45-2$^{\#}$ and 3$^{a\sim b}$ in S60-2$^{\#}$). Furthermore, the cracks initiation and coalescence (from point 1 to 2) cause obvious stress drops and intense AE events in both two specimens (S45-2$^{\#}$ and S60-2$^{\#}$), which is very different from the above S0-3$^{\#}$ and S30-3$^{\#}$ (relatively small stress drops and weak AE events occurred corresponding to point 1 and 2). For both S45-2$^{\#}$ and S60-2$^{\#}$ specimens, after the coalescence between the opening and two joints (i.e. after point 2), the axial stress can continue to grow again with the increase of axial deformation until the final failure, which is also very different from S0-3$^{\#}$ and S30-3$^{\#}$ (an immediate failure occurrs after point 2 in a short time).

As shown in Figure 8(e)∼(f). When $\beta = 75°$ and 90°, The coalescence between opening and inner joint tips were firstly formed by cracks 1$^{a\sim b}$ in both S75-2$^{\#}$ and S90-3$^{\#}$. Then, for S90-3$^{\#}$, cracks 2$^{a\sim b}$ appeared at the north and south poles of opening and coalesced with the inner joint tips, forming two smaller removable blocks. Afterwards, cracks 2∼3 in S75-2$^{\#}$ and cracks 3$^{a\sim c}$ in S90-3$^{\#}$ initiated from the outer joint tips and coalesced with the left and right sides of opening, forming two larger removable blocks on the upper-right and lower-left sides of opening. The final failure of specimens was caused by cracks 4$^{a\sim c}$ in S75-2$^{\#}$ and 4$^{a\sim d}$ in S90-3$^{\#}$ as well as surface spalling in both two specimens. Although the cracking evolution processes between S75-2$^{\#}$ and S90-3$^{\#}$ are similar, the AE characteristics are fairly different. It can be seen that the cracks initiation and coalescence (point 1 to 3) in S75-2$^{\#}$ caused obvious AE events, although the corresponding stress drops are smaller. However, both obvious stress drops and AE events can not be observed during the cracks initiation and coalescence process (from point 1 to 3) in the pre-peak stage of S90-3$^{\#}$. In post-peak stage, the AE counts caused by final failure of S90-3$^{\#}$ is much higher than that of S75-2$^{\#}$, implying a more intense and more sudden energy release of S90-3$^{\#}$, which is similar to that of intact specimens.

Based on the above analysis, it can be found that the cases of $\beta = 0°\sim30°$ and $\beta = 90°$ tend to be more dangerous to underground constructions for the rapid failure and concentrated energy release during post-peak stage. However, the cases of $\beta = 45°\sim75°$ provide good supporting opportunity for surrounding rock mass, because after the coalescence between opening and joints, the rock mass has both a strong bearing capacity and a lower energy accumulation.

4. Numerical modelling

Although the laboratory tests in the previous sections helped us understand the effect of ligament angle on the macroscopic strength, deformation, failure behavior and AE characteristics of sandstone specimens containing a circular opening and two intermittent joints, the distribution

and evolution of stress and displacement fields around the opening is still difficult to obtain only through physical tests. Which greatly limits our understanding of failure mechanism. Therefore, in this section, numerical simulation method (Particle Flow Code in two dimension, PFC^{2D}) has been adopted to further explore the meso-mechanical failure mechanism of H-J sandstone specimens under uniaxial compression.

4.1. *A simple introduction of particle flow code*

The discrete element method (DEM) was introduced by Cundall [31] for the analysis of rock mechanics. As a major DEM tool, PFC (particle flow code) models the movement and interaction of rigid circular particles, as described by Cundall and Strack [32]. In PFC^{2D}, the mechanical behavior of specimen is simulated by BPM (Bonded Particle model), which is a collection of non-uniform-sized circular rigid particles that may be bonded together at their contact points, as shown in Figure 9(a) [34]. For brittle rock materials such as sandstone, granite, marble etc., PBM (Parallel Bond Model) has been widely used to simulate the mechanical behavior of rock. A parallel-bond can be envisioned as a set of elastic springs with constant normal and shear stiffnesses, uniformly distributed over a rectangular cross-section lying on the contact plane and centered at the contact point, as shown in Figure 9(b) [35]. These springs act in parallel with the point-contact springs that are used to model particle stiffness at a point. Particle relative motion (controlled by Newton's second law) causes a force and a moment to develop within the bond material as a result of the parallel-bond existence. This force and moment act on the two bonded particles, and can be related to maximum normal and shear stresses acting within the bond material at the bond periphery. As shown in Figure 9(c) [35], if either of these maximum stresses exceeds its corresponding bond tensile/shear strength, the parallel bond breaks and a tensile/shear crack is generated. This characteristic enables the code to investigate the process of crack generation and propagation. Therefore, the method provides a useful tool for studying the failure mechanism of tested rock specimens.

4.2. *Model setup and micro-parameters calibration*

The establishment of PFC^{2D} models and calculation process are all based on the actural sandstone specimens size and loading procedure. The numerical specimens are 65 mm in width and 130 mm in height. The particle radius obeys a uniform distribution ranging from 0.3 mm to 0.5 mm. An intact numerical specimen contains 14862 particles and 35904 contacts, which are accurate enough to achieve stable and repeatable numerical solution. The entire numerical specimen is placed between two rigid walls (top wall and bottom wall), the contacts between the walls and particles are set to frictionless, avoiding the effect of end friction on the internal stress state of the specimen. The circular opening and joints in numerical H-J specimens are achieved by deleting particles at specific locations. The established numerical H-J specimens was shown in Figure 10. To guarantee a quasi-static loading process of uniaxial compression simulation, the top and bottom walls are applied with a loading rate of 0.05 'm/s'. It should be noted that the 'm/s' is just a default velocity format in PFC but not a real loading rate in laboratory experiment. The actual loading rate in PFC can be obtained by multiplying by 0.05 'm/s' and mechanical timestep (about 8.64×10^{-8} s/step in this research), that is about 4.32×10^{-6} mm/step meaning a slow enough loading rate.

In the numerical modelling, parallel-bond model (PBM) was adopted because of its advantages in simulating the mechanical behavior of brittle rock materials [33]. To obtain accurate and reliable numerical results, the reasonable values of model parameters in PFC are crucial. Regarding the evaluation of the rationality of the model parameters, we believe that if the stress-strain

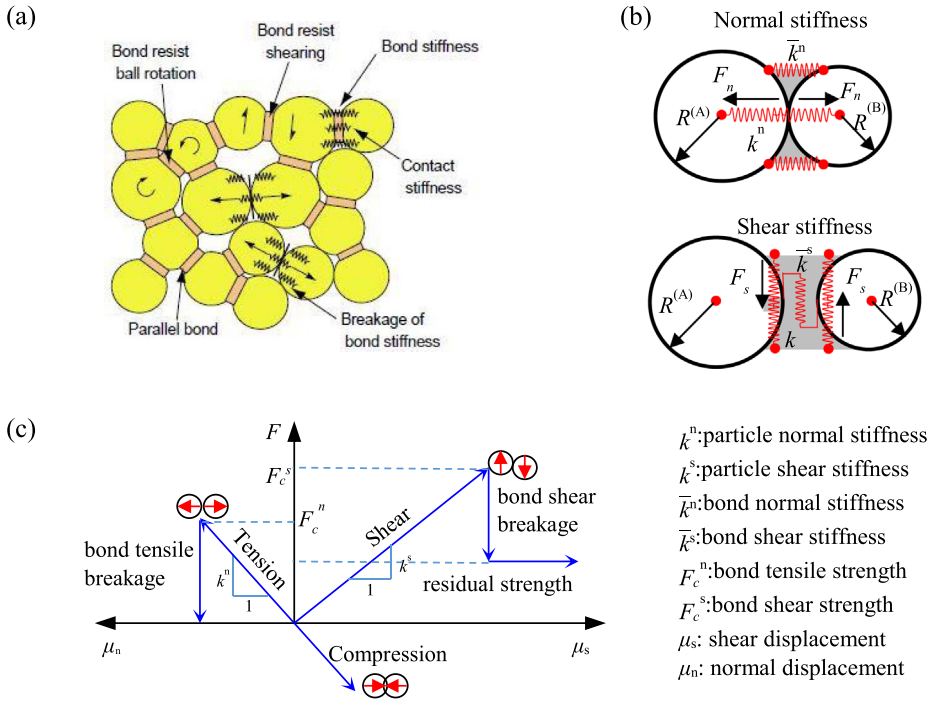

Figure 9. Bonded particle model (BPM) in PFC. (a) schematic representation of the bonded particle model [34]. (b) micro-scale properties of the bonded particle model [35]. (c) the mechanism of yielding bonds under normal and shear loads [35].

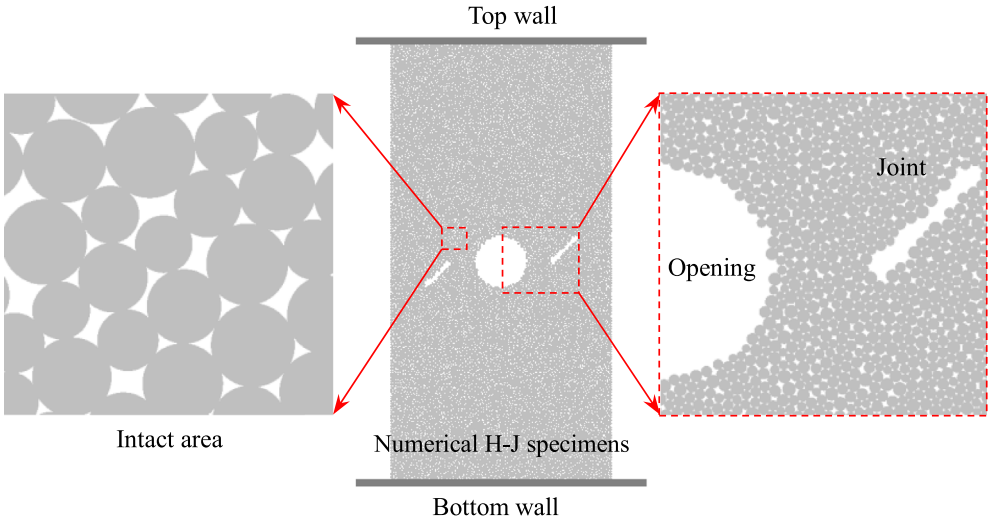

Figure 10. The established numerical H-J specimens using PFC^{2D}.

behaviors and failure characteristics of specimens obtained form numerical simulation are well consistent with the laboratory results under the same boundary conditions, the model parameters used are reasonable. In order to achieve this goal, the micro- parameters in PFC were checked

Table 2. The micro-parameters used in the PFC^{2D} model for sandstone in this research

Micro-parameter	Valve	Micro-parameter	Valve
Minimum radius, $R_{\min}$ (mm)	0.3	Young's modulus of the parallel bond, E_c^* (GPa)	3.50
Maximum radius, $R_{\max}$ (mm)	0.5	Ratio of normal to shear stiffness of the parallel bond,	1.25
Density, ρ (g/cm^3)	2390		
Particle friction coefficient, μ	0.3	Parallel-bond tensile strength, σ_t^* (MPa)	20.0
Young's modulus of the particle, E_c (GPa)	3.5	Parallel-bond cohesion, c^* (MPa)	38.0
Ratio of normal to shear stiffness of the particle,	1.25	Parallel-bond frictional angle, φ^* (°)	0.0

one by one through the method of 'trial and error'. In this research, the micro- parameters finally used in PFC for tested sandstone specimens are shown in Table 2.

Based on these micro-parameters listed in Table 2, numerical intact specimen and H-J specimens with different ligament angle were used to conduct uniaxial compression modelling tests. Figure 11 shows the comparison of stress-strain curves between laboratory tests and numerical modelling. It can be seen that the stress-strain curves obtained from PFC are in good agreement with the test results both for intact specimen and H-J specimens. The elastic deformation stage, stress drops and fluctuations caused by cracks initiation and coalescence, as well as the brittle failure after peak strength are all well reproduced by numerical modelling. However, the initial compaction stage appeared in tested stress-strain curves can not be simulated by PFC.

Figure 12 shows the comparison of strength and deformation parameters between laboratory tests and numerical modelling. It can be seen that the simulated peak strengths of H-J specimens with different ligament angle are very consistent with the test results, except for a slightly higher at $\beta = 15°$ and a slightly lower at $\beta = 90°$, as shown in Figure 12(a). However, as shown in Figure 12(b), the simulated values of elastic modulus under different ligament angle are all higher than the tested values and have a smaller change as the ligament angle increases, which may be because the two-dimensional simulation limits the deformation in the normal direction of the plane, thereby improving the in-plane deformation stiffness. In addition, it can be seen from Figure 12(c) that the trend of simulated peak strain with ligament angle is well consistent with the test results, but the simulated values are much smaller than test results due to the lack of initial compaction stage in numerical modelling. By adding the initial compaction strain ε_0, which is determinated in Figure 11, the revised simulated peak strain values are well consistent with the tested results.

Figure 13 shows the comparison of ultimate failure modes between numerical modelling and laboratory tests. It can be seen that all three types of coalescence failure modes (Mode I, II and III observed in Section 3.2) can be reproduced to a large extent in PFC. Some differences between numerical results and test results are mainly reflected by the coalescence failure between the outer joint tips and specimen boundaries, which is mainly because the established numerical specimens can not fully reflect the microscopic heterogeneity of real sandstone specimens.

4.3. *Stress field characteristics just before crack initiation*

The cracking analysis in Section 3.2 has revealed that the coalescence failures between joints and opening are obviously dependent on the ligament angle, implying different mechanical

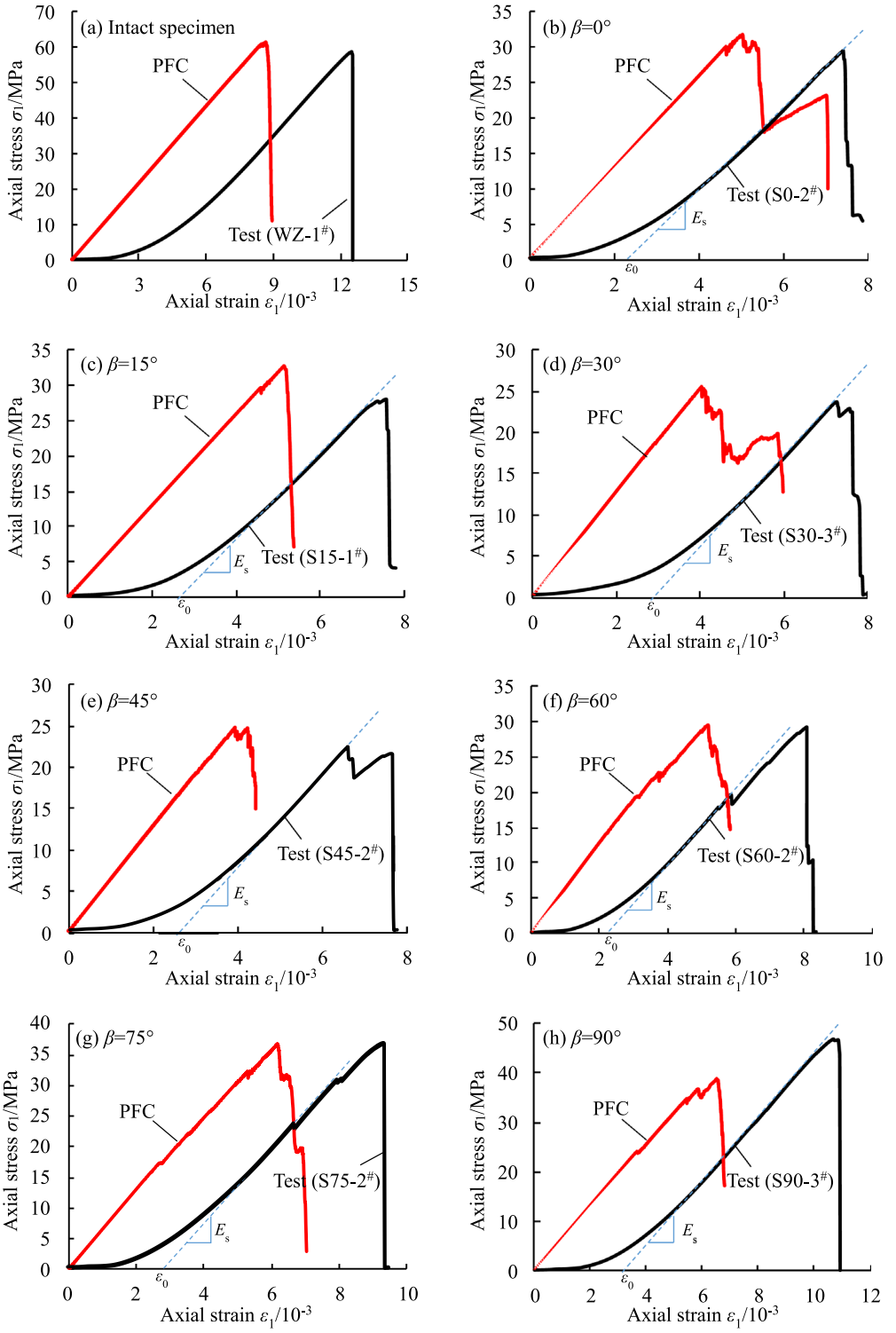

Figure 11. Comparison of stress-strain curves between laboratory tests and numerical simulation.

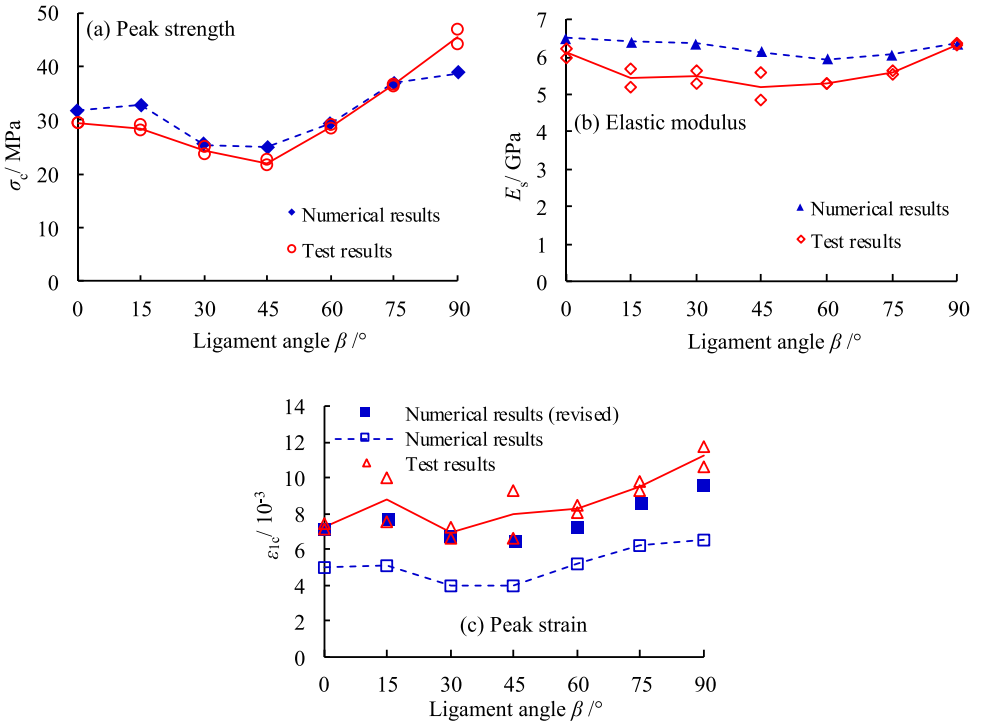

Figure 12. Comparison of strength and deformation parameters between laboratory tests and numerical simulation. (a) Peak strength. (b) Elastic modulus. (c) Peak strain.

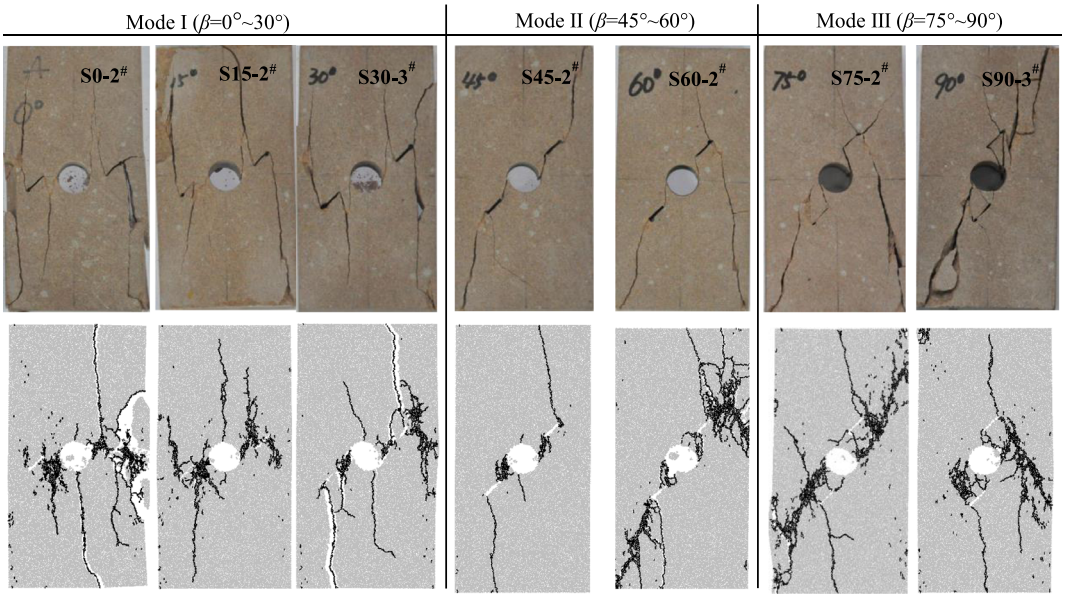

Figure 13. Comparison of ultimate failure modes between laboratory tests and numerical simulation.

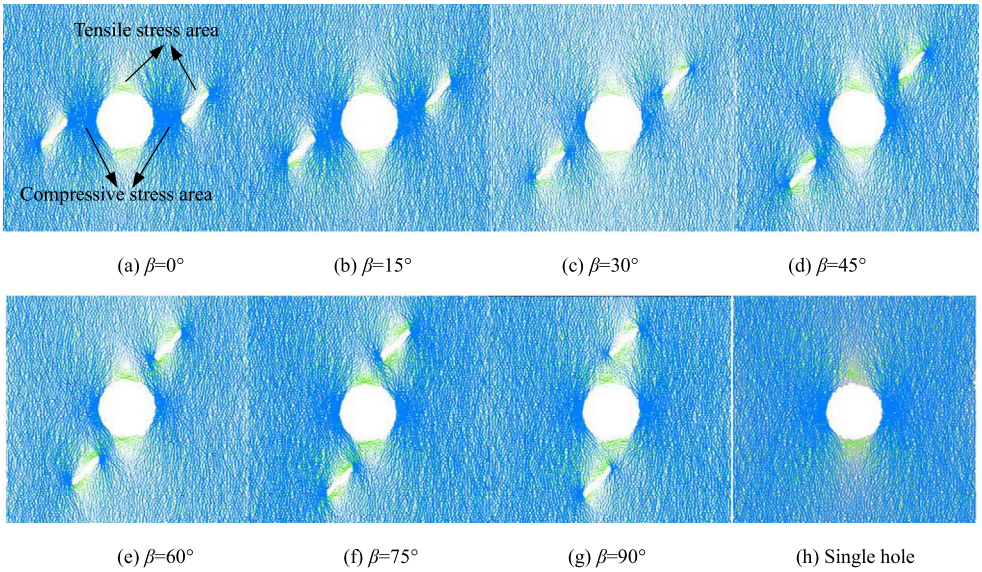

Figure 14. The local stress field around opening and joints just before cracks initiation.

interaction between opening and joints with different positions. Therefore, the stress distribution around the opening under different joint positions should be better understood. In PFC, the stress in bonded particle model can be represented by the contact forces acting on the parallel-bonds. Figure 14 shows the local stress fields around the circular opening and joints just before cracks initiation, in which the green lines stands for tensile forces and the blue lines stand for compressive forces. The higher intensity distribution of lines segments indicates a higher stress field. In addition, to quantitatively represent the changes of stress field around opening caused by different ligament angle, 12 measurement spheres in PFC were arranged around the circular opening in a anticlockwise order starting from the right side of opening at an angular interval of 30°, as shown in Figure 15. It should be noted that stress, as a continuous variable, does not actually exist in the discrete models created by PFC. The stress of one point measured by measurement sphere is in fact an average value in the measurement area. Therefore, the diameter of measurement sphere is crucial for obtaining accurate stress values. In this research, the diameter of every measurement sphere is set to 4 mm, with each measurement region enclosing an average of 24 balls, which is accurate enough according to previous studies [20, 21]. Based on the measured stress components of one point, the principal stress (i.e. maximum principal stress, $\sigma_{\max}$ and minimum principal stress, $\sigma_{\min}$ in two-dimensional models) can be calculated. The distribution of $\sigma_{\max}$ and $\sigma_{\min}$ around the opening in H-J specimens with different ligament angle is shown in Figure 16. Note that positive values indicate tension and negative values indicate compression.

As can be clearly seen from Figure 14, the tensile stress areas are mainly located in the top and bottom of circular opening as well as the middle-upper and middle-lower parts of joint faces, while the compressive stress areas are mainly concentrated at two sides of opening and tip positions of joints. When the ligament angle is smaller ($\beta = 0° \sim 30°$), the compressive stress at two sides of opening and joint tips overlap each other, resulting a highly compressive stress state in rock bridge area, which may explain why there is no a direct coalescence in the rock bridge area. When the ligament angle increases to 45°, the compressive stress fields at inner joint tips begin to detach from the sides of opening. The reduction of compressive stress in rock bridge area

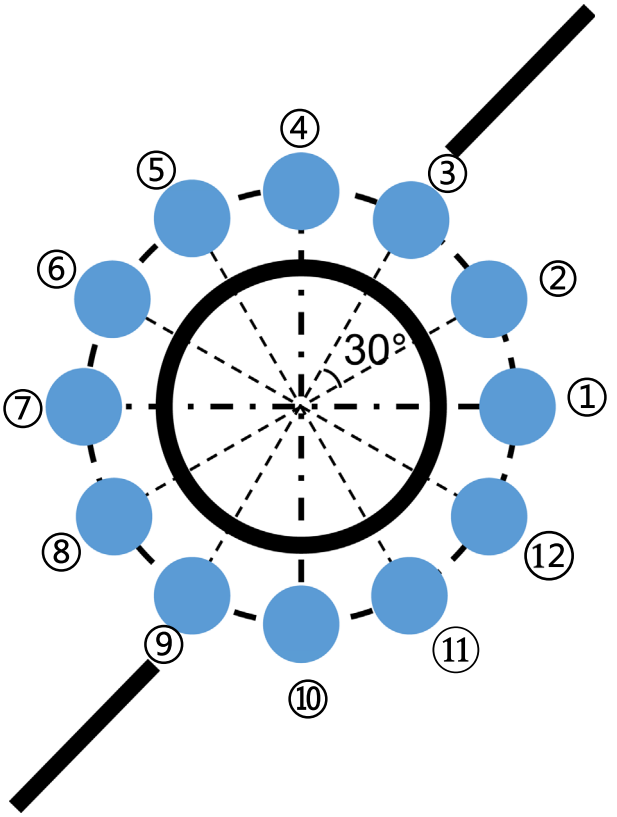

Figure 15. The arrangement of measurement spheres around circular opening in H-J specimens.

makes a direct coalescence possile, which has been evidenced by the single crack coalescence in rock bridge area for $\beta = 45°$ and 60°. When $\beta = 75°$ and 90°, the tensile stress areas at the middle-upper and middle- lower parts of joints get merged (not overlapped) with the tensile stress areas at the top and bottom of opening. The merged tensile stress areas tend to be well consistent with the scope of removable blocks appeared in the failed specimens with $\beta = 75°$ and 90° (shown in Figure 7). More can be seen from Figure 16 that, the change of ligament angle will not obviously change the distribution of compressive and tensile stress area around the opening. At any ligament angle, the compressive stress area are mainly located in the scope of ②①⑫ and ⑥⑦⑧, while the tensile stress area are mainly locates in the scope of ③④⑤ and ⑨⑩⑪. However, the magnitude of $\sigma_{\max}$ changes greatly with the change of ligament angle. The maximum $\sigma_{\max}$ occurrs at $\beta = 0°$ in position ① (44.9 MPa) and ⑦ (38.5 MPa), which is the results of compressive stress overlap. When $\beta = 45°$ and 60°, the $\sigma_{\max}$ decreases to 19.8 Mpa at ① and 18.0 Mpa at ⑦, indicating a lower compressive stress state in rock bridge area. However, $\sigma_{\min}$ has a little change with ligament angle even when $\beta = 90°$, indicating that no obvious tensile stress overlap occurred between the opening and joints.

4.4. *Local stress evolution characteristics*

To further reveal stress changes around the opening during the cracking process, the maximum and minimum principal stress were monitored by 12 measure spheres around the opening, as

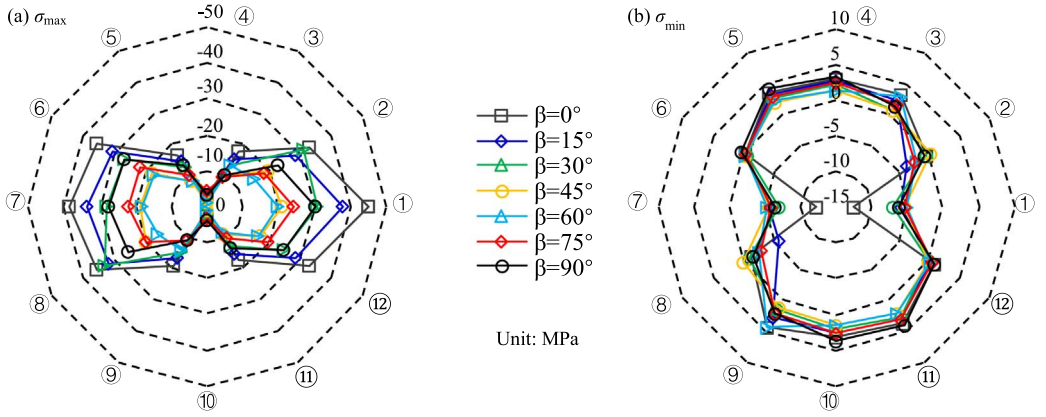

Figure 16. The principal stress distribution around a circular opening for H-J specimens with different ligament angle. (a) Maximum principal stress, σ_{max}. (b) Minimum principal stress, σ_{min}.

shown in Figure 15. The local principal stress evolution curves and overall stress-strain curves and cracking process were shown in Figure 17 ($\beta = 0°$), Figure 18 ($\beta = 45°$) and Figure 19 ($\beta = 90°$). The numerical results showed that local principal stress evolution is highly corresponding to the rupture process of H-J specimens. Several main features can be summarized below:

- The cracks initiation from top/bottom of opening (point 1 of $\beta = 0°$ and 90°) and joint tips (point 1 of $\beta = 45°$) always cause obvious minimum principal stress fluctuations. The cracks propagation on the top and bottom of opening caused obvious reduction of minimum principal stress in the tensile stress area (i.e. ③④⑤ and ⑨⑩⑪), e.g. point 3 of $\beta = 0°$ and point 3~4 of $\beta = 90°$. However, the generation of cracks on the opening side always resulted in a sudden increase of minimum principal stress, e.g. point 2 in each case, indicating a compressive stress concentration on the opening side.
- The coalescence between the opening and joints caused obvious changes of maximum principal stress in rock bridge area. When $\beta = 0°$ (Figure 17), the maximum principal stress on right side of opening (i.e. ⑫①②) began to decrease at point 4, then to a low level at point 5 and finally to zero at point 6, indicating a complete loss of bearing capacity of right side of opening. Therefore, the overall stress-strain curve showed a rapid decrease from point 5 to 6, which explains the rapid failure after coalescence observed by test results shown in Figure 8(a)~(b).
- At point 4 of $\beta = 45°$ (in Figure 18) and point 6 of $\beta = 90°$ (in Figure 19), the coalescence between opening and joint also caused obvious reduction of maximum principal stress on right side of opening (i.e. ①②⑫). However, the reduction degree is ①: 8.85% ②: 25.4% ⑫: 33.5% when $\beta = 45°$ and ①: 36.1% ②: 100% (drop to 0) ⑫: 30.6% when $\beta = 90°$, indicating that the right opening side still has a certain bearing capacity, not a complete loss. Therefore, the overall stress-strain curve showed a small drop then increased again, as shown in point 4~5 of $\beta = 45°$ and point 6~7 of $\beta = 90°$. This is fairly consistent with the test results in Figure 8(c)~(e).
- When $\beta = 0°$, the complete loss of bearing capacity on right side of opening resulted in the obvious increase of maximum principal stress on left side (i.e. ⑥⑦⑧), indicating the left side of opening has become the main bearing area. However, when $\beta = 45°$ and 90°, no obvious increase of maximum principal stress on left side was observed caused by the stress reduction of right side of opening. The principal stress on both left and right sides

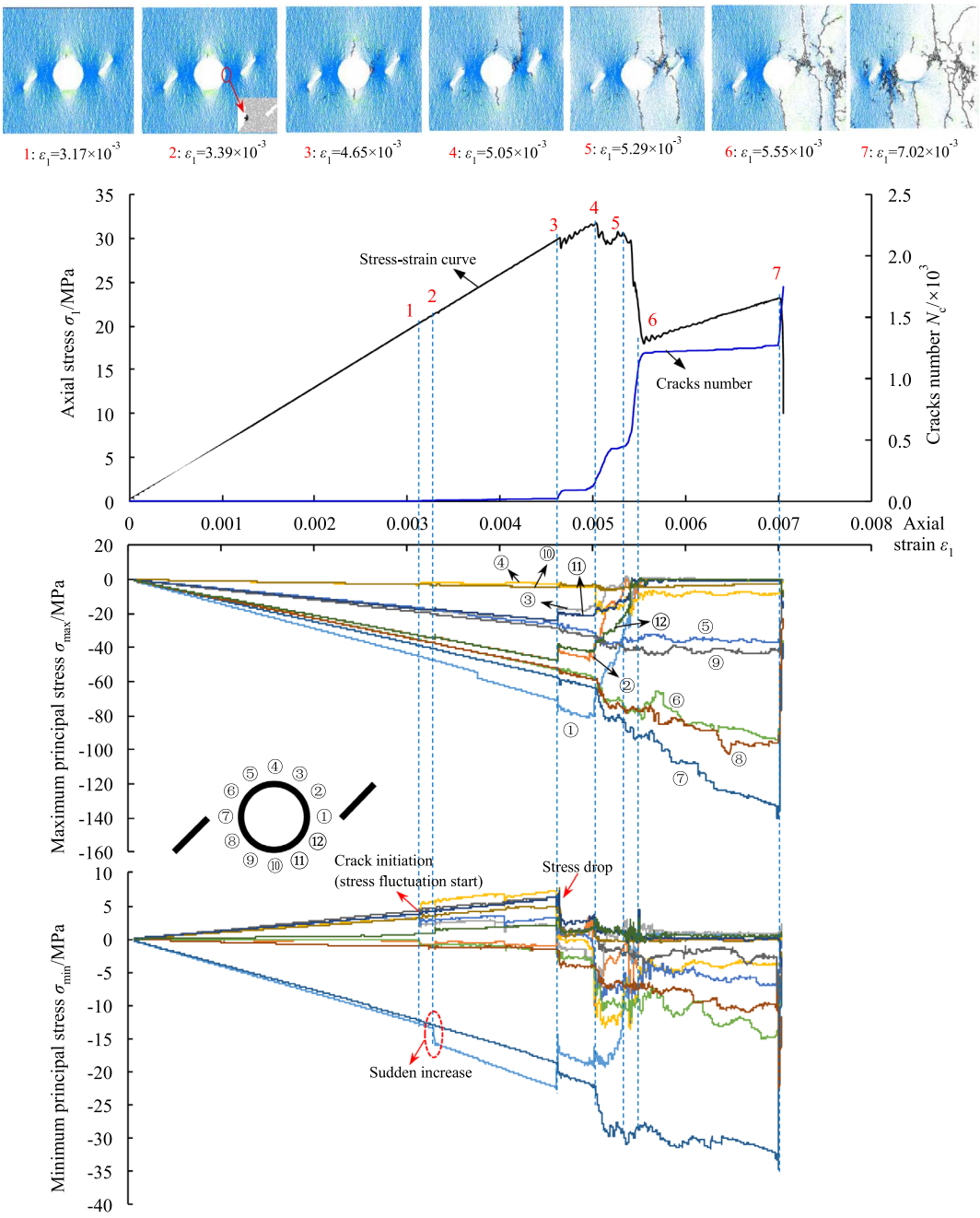

Figure 17. The stress-strain curve, cracking process and local principal stress evolution around the opening during the uniaxial loading process, $\beta = 0°$.

of opening finally decreased to a low level after the coalescence occurred between joint and left side of opening.

Based on the above analysis, it can be concluded that the stress-strain curve of specimens is essentially a comprehensive reflection of the local stress evolution, especially the maximum

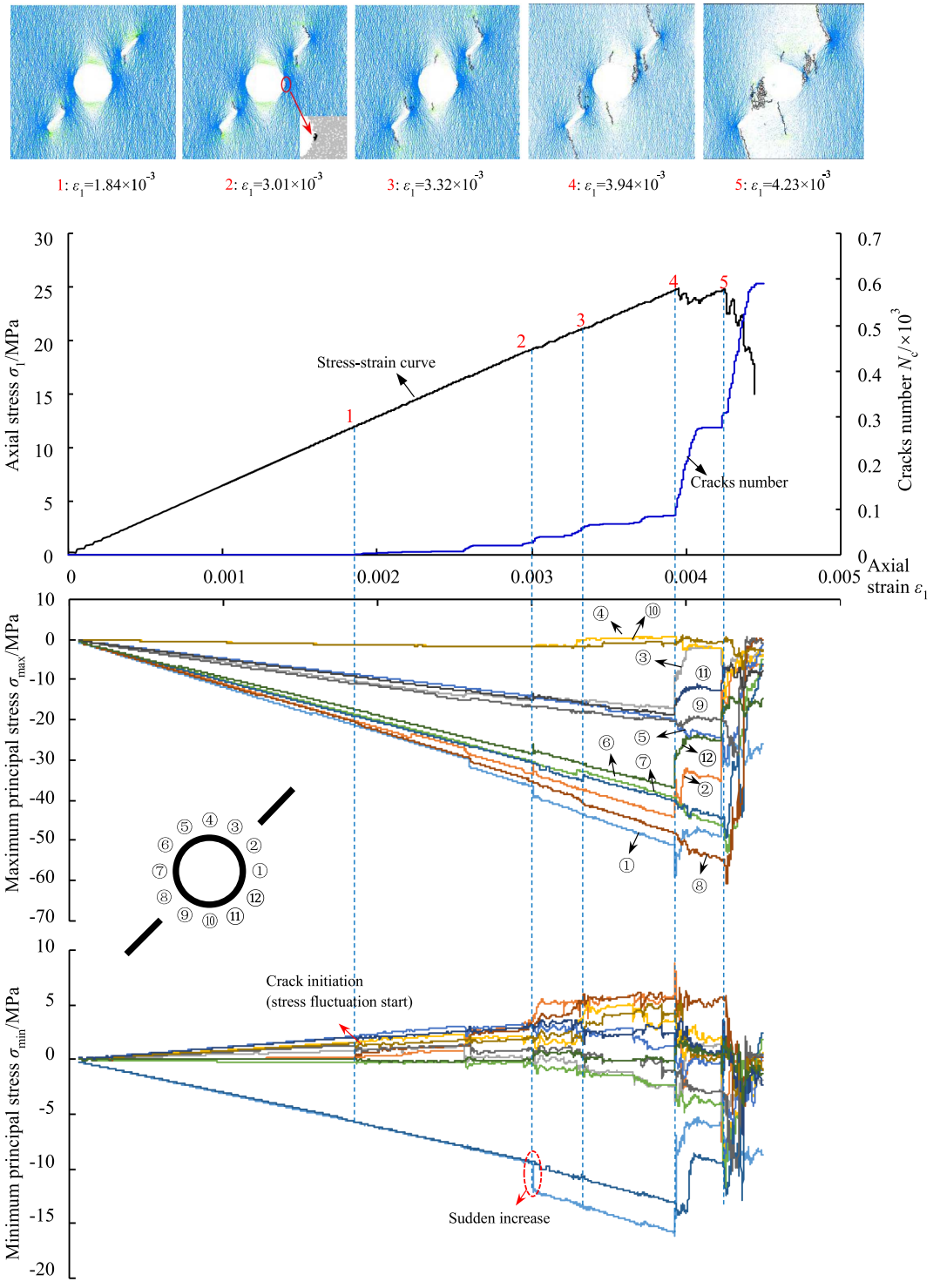

Figure 18. The stress-strain curve, cracking process and local principal stress evolution around the opening during the uniaxial loading process, $\beta = 45°$.

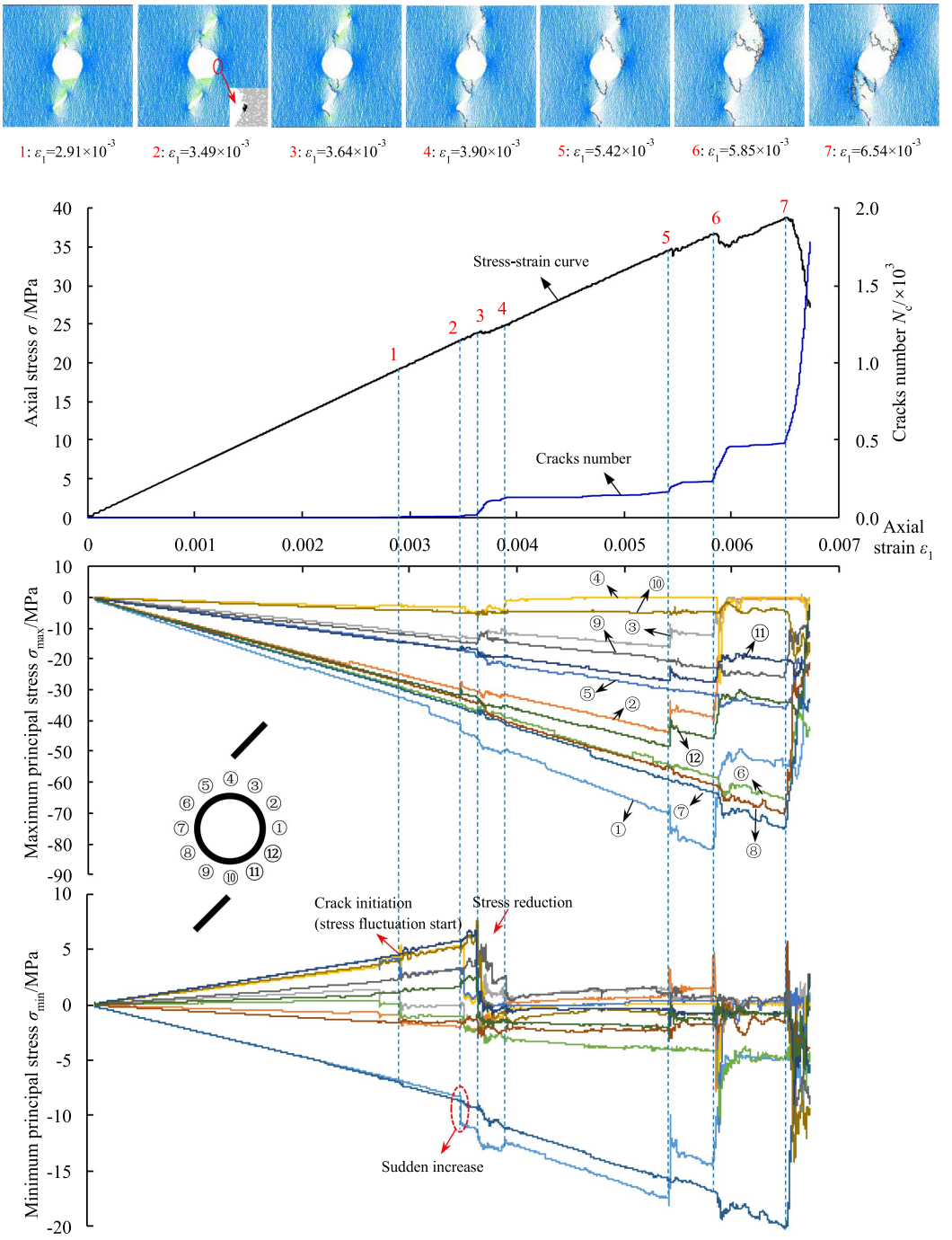

Figure 19. The stress-strain curve, cracking process and local principal stress evolution around the opening during the uniaxial loading process, $\beta = 90°$.

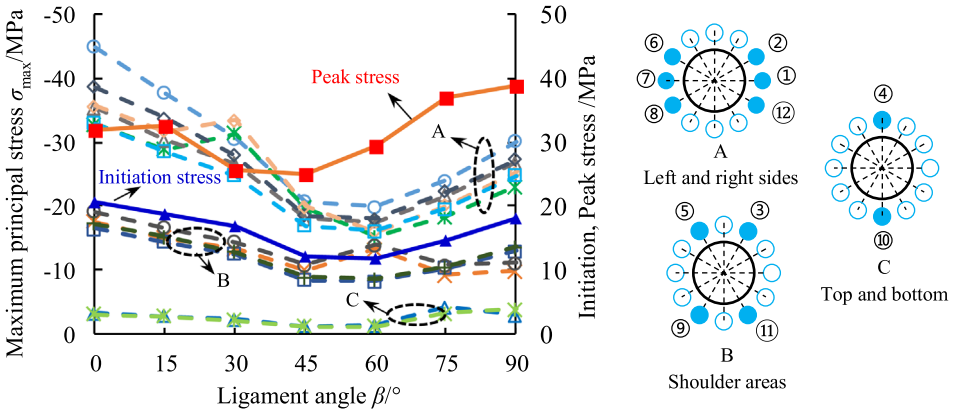

Figure 20. The relationship between local maximum principal stress around the opening and strength of H-J specimens.

principal stress. The cracks initiation and propagation, although cause fluctuations, drops or increases of local minimum principal stress, have little effect on local maximum principal stress and the overall stress-strain curve of the specimen. It is the occurrence of crack coalescence between the opening and joints that caused large stress reduction of local maximum principal stress, correspondingly caused the obvious stress drops of the stress-strain curve and rapid increase of crack number. The left and right sides are the most important bearing areas around the opening, the coalescence failure between two sides and joints eventually leads to the loss of bearing capacity of specimens.

Furthermore, to some extent, the local stress field around the opening can reflect the strength characteristics of H-J specimens. For example, the initiation stress and peak stress of H-J specimens can be reflected by the local maximum principal stress around the opening just before crack initiation, as shown in Figure 20. It seems that the peak stress can be reflected by the maximum principal stress on the left and right sides (i.e. the region of ⑥⑦⑧ and ⑫①②). In particular, a good consistency occurs when $\beta < 45°$. However, the initiation stress tends to be more related to the maximum principal stress of shoulder area (i.e. the region of ③,⑤,⑨,⑪). A good consistency can be found at any ligament angle from 0°~90°. This indicates that local stress monitoring on the shoulders and two sides of opening can be great significance for evaluating the stability of surrounding rock mass.

5. Local displacement characteristics

To further understand the relationship between stress evolution characteristics and cracking around the opening, the coalescence failure mechanism between the opening and surrounding joints has been revealed from the perspective of local displacement fields, as shown in Figure 21. In which, the displacement of one particle is indicated by the magnitude and direction of the arrow acting on this particle. The local displacement fields of the failed bridge area are shown in the enlarged views. Based on the relative motion relationship of particles on both sides of fracture surface, four kinds of displacement modes can be observed:

(1) Direct tension mode (DT). The fracture is caused by the opposite movement trend of particles along the normal direction of the fracture surface.
(2) Relative tension mode (RT). Although the movement trend of particles along the normal direction of fracture surface is the same, the magnitude difference of displacement can still result in the tensile fractures.

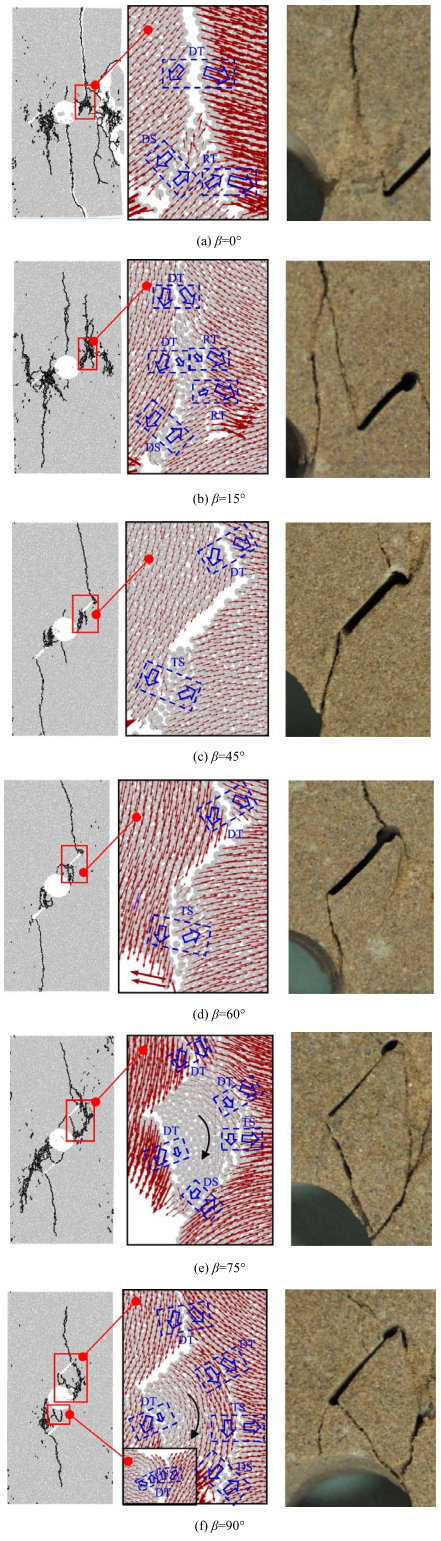

Figure 21. Local displacement fields of coalescence areas between the opening and joints.

(3) Direct shear mode (DS). The fracture is caused by the opposite movement trend of particles along the tangential direction of the fracture surface.
(4) Tensile shear mode (TS). Which is in fact a coexistence of direct or relative tension along the normal direction of fracture and direct shear along the tangential direction of fracture surface.

It can be seen from Figure 21(a)~(b) that the indirect coalescence between the opening and joints is essentially composed of DS, DT and RT. Combined with Figure 17, we can know that the direct shear cracks usually initiate at the right and left sides of opening and propagate obliquely to a certain distance, then convert into direct tensile cracks and propagate in the direction of uniaxial loading. The relative tensile cracks initiate at the inner tips of joints and propagate in the approximately vertical direction and finally coalesce with the direct tensile cracks, resulting in a inverted Y-type coalescence between the opening and joints. In addition, the shear cracks are usually smoother and also accompanied by small broken rock debris in the fracture surfaces, while the tensile cracks usually have a larger roughness and obvious aperture. Which can be observed in both numerical modelling and test results.

Figure 21(c)~(d) shows that the single crack coalescence between the opening and joints occurred at $\beta = 45°$ and 60° is caused by TS. Compared with the direct shear cracks, the tensile shear cracks tend to have both obvious shear displacement and a certain degree of crack aperture.

Figure 21(e)~(f) shows that the multiple cracks coalescence (removable blocks coalescence) between the opening and joints occurred at $\beta = 75°$ and 90° is composed of DT, TS and DS. The small removable blocks located on the top and bottom of opening formed by two direct tensile cracks connecting the inner joint tips and the top, bottom of opening. However, the larger removable blocks located on the upper right and lower left sides of opening formed by the curved crack connecting the outer joint tips and right, left sides of opening. Under the action of rotational displacement of the larger blocks, the curved cracks tend to be direct shear cracks near the opening, then transform into tensile shear cracks in the middle parts, and eventually become direct tensile cracks near the outer joint tips.

Combined with the stress evolution analysis in Section 4.4, it can be found that different cracking mechanism may cause different local stress changes and finally determines the overall mechanical behavior of specimens. For example, the indirect coalescence caused by DT and RT at $\beta = 0°$ tend to rapidly reduce the maximum principal stress on the opening side, finally leading to a complete loss of bearing capacity of opening side. However, a certain bearing capacity of opening side at $\beta = 45°$ and 90° can be reserved after coalescence by TS ($\beta = 45°$) and TS, DS ($\beta = 90°$). The residual bearing capacity of opening side may be offered by the frictional effect of shear plane ($\beta = 45°$) and removable block rotational impedance ($\beta = 90°$).

6. Conclusions

In this research, the effect of different positions of joints around the opening on the failure and mechanical behavior of sandstone specimens containing a circular opening and two open joints (called H-J sandstone specimens in this study) were explored by changing the ligament angle. Based on the experiment and numerical simulation, the effect of ligament angle on strength, deformation, cracking process, local stress distribution and evolution of H-J sandstone specimens were detailedly analysed. Several meaningful conclusions can be concluded as follows:

(1) The strength and deformation paramaters of H-J sandstone specimens are highly dependent on the ligament angle. Both the peak strength and elastic modulus firstly decrease then increase with the increasing ligament angle, and the minimum values occurs at $\beta = 45°$. However, the influence degree of ligament angle on elastic modulus is much

less than that on peak strength. Generally, the peak strain increases with the increasing ligament angle.

(2) The cracking process and AE characteristics of H-J specimens were related to ligament angle. When $\beta = 0°\sim30°$, the main rupture process occurs in the post-peak stage. The crack initiation and coalescence cause small stress drops and weak AE events, while an intense and rapid failure is caused by the coalescence failure between the outer joint tips and specimen boundaries. When $\beta = 45°\sim60°$, obvious AE events and stress drops caused by crack initiation and coalescence can be observed. After the coalescence, the specimens still have strong bearing capacity, rather than an immediate failure. The AE characteristics of $\beta = 75°$ is similar to that of $\beta = 45°$ and $60°$ despite the different cracking process. However, when $\beta = 90°$, both obvious stress drops and AE events can not be observed in the pre-peak stage, the accumulated energy tends to be released instantaneously in the post-peak stage, resulting in an intense failure similar to that of intact specimens.

(3) The local stress state around the opening is highly influenced by the ligament angle. The local compressive stress overlap at $\beta = 0°\sim30°$, the compressive stress detachment at $\beta = 45°\sim60°$ and the tensile stress mergence at $\beta = 75°\sim90°$ can be responsible for different coalescence failures between the opening and joints. The local stress evolution around the opening is highly corresponding to the cracking process. The initiation and propagation of microcracks caused obvious local minimum principal stress fluctuations, drops or increases, while having little effect on the local maximum principal stress and overall stress-strain curve. The reduction of maximum principal stress at left and right sides of opening caused by the crack coalescence was the main reason for the bearing capacity loss of the specimens.

(4) Three types of coalescence failure patterns can be identified from both experimental and numerical results, i.e. indirect coalescence (mode I), single crack coalescence (mode II) and multiple crack coalescence (or removable blocks coalescence, mode III). According to the relative displacement relation of particles, Mode I was mainly caused by DS, DT and RT, mode II was caused by TS, while mode III was caused by DS, TS and DT. (DT-direct tension; RT-relative tension; TS-tensile shear; DS-direct shear). Different cracking mechanisms are accompanied by different local stress changes, which finally determines the overall bearing capacity of rock mass.

Acknowledgements

This research was supported by China Scholarship Council (File No. 201806420027). Special thanks to state key laboratory for geomechanics and deep underground engineering, china university of mining and technology for providing the experimental equipments. The authors would like to express their sincere gratitude to the editor and reviewers for their valuable comments, which have greatly improved this paper.

Conflicts of Interest

The authors declare no conflict of interest.

References

[1] E. Hoek, E. T. Brown, “Practical estimates of rock mass strength”, *Int. J. Rock Mech. Min. Sci.* **34** (1997), p. 1165-1186.

[2] E. Z. Lajtai, B. J. Carter, E. J. S. Duncan, "En echelon crack-arrays in potash salt rock", *Rock Mech. Rock Eng.* **27** (1994), p. 89-111.
[3] E. Z. Lajtai, "Brittle fracture in compression", *Int. J. Fracture* **10** (1974), p. 525-536.
[4] L. N. Y. Wong, H. H. Einstein, "Systematic evaluation of cracking behavior in specimens containing single flaws under uniaxial compression", *Int. J. Rock Mech. Min. Sci.* **46** (2009), p. 239-249.
[5] R. H. C. Wong, K. T. Chau, "Crack coalescence in a rock-like material containing two cracks", *Int. J. Rock Mech. Min. Sci.* **35** (1998), p. 147-164.
[6] P. Yin, R. H. C. Wong, K. T. Chau, "Coalescence of two parallel pre-existing surface cracks in granite", *Int. J. Rock Mech. Min. Sci.* **68** (2014), p. 66-84.
[7] S. Q. Yang, X. R. Liu, H. W. Jing, "Experimental investigation on fracture coalescence behavior of red sandstone containing two unparallel fissures under uniaxial compression", *Int. J. Rock Mech. Min. Sci.* **63** (2013), p. 82-92.
[8] X. P. Zhang, Q. S. Liu, S. C. Wu, X. H. Tang, "Crack coalescence between two non-parallel flaws in rock-like material under uniaxial compression", *Eng. Geol.* **199** (2015), p. 74-90.
[9] S. Q. Yang, "Crack coalescence behavior of brittle sandstone samples containing two coplanar fissures in the process of deformation failure", *Eng. Fract. Mech.* **78** (2011), p. 3059-3081.
[10] L. N. Y. Wong, H. Q. Li, "Numerical study on coalescence of two pre-existing coplanar flaws in rock", *Int. J. Solids Struct.* **50** (2013), p. 3685-3706.
[11] M. Prudencio, M. V. S. Jan, "Strength and failure modes of rock mass models with non-persistent joints", *Int. J. Rock Mech. Min. Sci.* **44** (2007), p. 890-902.
[12] M. Chen, S. Q. Yang, P. G. Ranjith, W. D. Yang, P. F. Yin, Y. C. Zhang, Q. Y. Zhang, "Fracture processes of rock-like specimens containing nonpersistent fissures under uniaxial compression", *Energies* **12** (2018), p. 79.
[13] E. Z. Lajtai, B. J. Carter, E. J. S. Duncan, "Mapping the state of fracture around cavities", *Eng. Geol.* **31** (1991), p. 277-289.
[14] C. D. Martin, R. S. Read, J. B. Martino, "Observations of brittle failure around a circular test tunnel", *Int. J. Rock Mech. Min. Sci.* **34** (1997), p. 1065-1073.
[15] S. Jeon, J. Kim, Y. Seo, C. Hong, "Effect of a fault and weak plane on the stability of a tunnel in rock-a scaled model test and numerical analysis", *Int. J. Rock Mech. Min. Sci.* **41** (2004), p. 658-663.
[16] Y. H. Hao, R. Azzam, "The plastic zones and displacements around underground openings in rock masses containing a fault", *Tunn. Undergr. Space Technol.* **20** (2005), p. 49-61.
[17] S. Yan, J. B. Bai, W. F. Li, J. G. Chen, L. Li, "Deformation mechanism and stability control of roadway along a fault subjected to mining", *Int. J. Min. Sci. Technol.* **22** (2012), p. 559-565.
[18] M. Sagong, D. Park, J. Yoo, J. S. Lee, "Experimental and numerical analyses of an opening in a jointed rock mass under biaxial compression", *Int. J. Rock Mech. Min. Sci.* **48** (2011), p. 1055-1067.
[19] S. Q. Yang, T. Xu, L. He, H. W. Jing, S. Wen, Q. L. Yu, "Numerical study on failure behavior of brittle rock specimen containing pre-existing combined flaws under different confining pressure", *Arch. Civ. Mech. Eng.* **15** (2015), p. 1085-1097.
[20] T. Liu, B. Q. Lin, W. Yang, Q. L. Zou, J. Kong, F. Z. Yan, "Cracking process and stress field evolution in specimen containing combined flaw under uniaxial compression", *Rock Mech. Rock Eng.* **49** (2016), p. 3095-3113.
[21] X. Fan, K. H. Li, H. P. Lai, Y. L. Xie, R. H. Cao, J. Zheng, "Internal stress distribution and cracking around flaws and openings of rock block under uniaxial compression: A particle mechanics approach", *Comput. Geotech.* **102** (2018), p. 28-38.
[22] F. Feng, X. B. Li, J. Rostami, D. Y. Li, "Modeling hard rock failure induced by structural planes around deep circular tunnels", *Eng. Fract. Mech.* **205** (2019), p. 152-174.
[23] R. H. C. Wong, P. Lin, C. A. Tang, K. T. Chau, "Creeping damage around an opening in rock-like material containing non-persistent joints", *Eng. Fract. Mech.* **69** (2002), p. 2015-2027.
[24] F. Chen, Z. Sun, J. Xu, "Mode i fracture analysis of the double edge cracked brazilian disk using a weight function method", *Int. J. Rock Mech. Min. Sci.* **3** (2001), p. 475-479.
[25] L. Tutluoglu, C. Keles, "Mode i fracture toughness determination with straight notched disk bending method", *Int. J. Rock Mech. Min. Sci.* **48** (2011), p. 1248-1261.
[26] C. S. Chen, P. Ernian, A. Bernard, "Fracture mechanics analysis of cracked discs of anisotropic rock using the boundary element method", *Int. J. Rock Mech. Min. Sci.* **35** (1998), p. 195-218.
[27] C. C. Ke, C. S. Chen, C. H. Tu, "Determination of fracture toughness of anisotropic rocks by boundary element method", *Rock Mech. Rock Eng.* **41** (2006), p. 509-538.
[28] C. A. Tang, R. H. C. Wong, K. T. Chau, P. Lin, "Modeling of compression-induced splitting failure in heterogeneous brittle porous solids", *Eng. Fract. Mech.* **72** (2005), p. 597-615.
[29] R. H. C. Wong, P. Lin, C. A. Tang, "Experimental and numerical study on splitting failure of brittle solids containing single pore under uniaxial compression", *Mech. Mater.* **38** (2006), p. 142-159.
[30] T. Xu, P. G. Ranjith, P. L. P. Wasantha, J. Zhao, C. A. Tang, W. C. Zhu, "Influence of the geometry of partially-spanning joints on mechanical properties of rock in uniaxial compression", *Eng. Geol.* **167** (2013), p. 134-147.

[31] P. A. Cundall, "A computer model for simulating progressive large scale movements in blocky rock systems", in *Proceedings of the Symposium of International Society of Rock Mechanics, Nancy, France*, vol. 1, Society for Rock Mechanics (ISRM), 1971, II-8.
[32] P. A. Cundall, O. D. L. Strack, "A discrete numerical model for granular assemblies", *Geotechnique* **29** (1979), p. 47-65.
[33] D. O. Potyondy, P. A. Cundall, "A bonded-particle model for rock", *Int. J. Rock Mech. Min. Sci.* **41** (2004), p. 1329-1364.
[34] N. Cho, C. D. Martin, D. C. Sego, "A clumped particle model for rock", *Int. J. Rock Mech. Min. Sci.* **44** (2007), p. 997-1010.
[35] M. Bahaaddini, P. C. Hagan, R. Mitra, B. K. Hebblewhite, "Parametric study of smooth joint parameters on the shear behaviour of rock joints", *Rock Mech. Rock Eng.* **48** (2015), p. 923-940.
[36] S. Q. Yang, M. Chen, H. W. Jing, K. F. Chen, B. Meng, "A case study on large deformation failure mechanism of deep soft rock roadway in Xin' An coal mine, China", *Eng. Geol.* **217** (2017), p. 89-101.
[37] X. L. Zhang, Y. Y. Jiao, J. Zhao, "Simulation of failure process of jointed rock", *J. Cent. South Univ. Technol.* **15** (2008), p. 888-894.
[38] Y. S. Xie, P. Cao, J. Liu, L. W. Dong, "Influence of crack surface friction on crack initiation and propagation: A numerical investigation based on extended finite element method", *Comput. Geotech.* **74** (2016), p. 1-14.
[39] X. P. Zhang, L. N. Y. Wong, "Cracking processes in rock-like material containing a single flaw under uniaxial compression: A numerical study based on parallel bonded-particle model approach", *Rock Mech. Rock Eng.* **45** (2011), p. 711-737.
[40] J. Jin, P. Cao, Y. Chen, C. Z. Pu, D. W. Mao, X. Fan, "Influence of single flaw on the failure process and energy mechanics of rock-like material", *Comput. Geotech.* **86** (2017), p. 150-162.
[41] S. Q. Yang, Y. H. Huang, "Failure behaviour of rock-like materials containing two pre-existing unparallel flaws: An insight from particle flow modeling", *Eur. J. Environ. Civ. Eng.* **22** (2018), p. s57-s78.
[42] X. Fan, P. H. S. W. Kulatilake, X. Chen, "Mechanical behavior of rock-like jointed blocks with multi-non-persistent joints under uniaxial loading: A particle mechanics approach", *Eng. Geol.* **190** (2015), p. 17-32.
[43] C. Cheng, X. Chen, S. F. Zhang, "Multi-peak deformation behavior of jointed rock mass under uniaxial compression: Insight from particle flow modeling", *Eng. Geol.* **213** (2016), p. 25-45.
[44] X. X. Yang, H. W. Jing, K. F. Chen, S. Q. Yang, "Failure behavior around a circular opening in a rock mass with non-persistent joints: A parallel-bond stress corrosion approach", *J. Cent. South Univ.* **24** (2017), p. 2406-2420.
[45] S. Q. Yang, P. F. Yin, Y. C. Zhang, M. Chen, X. P. Zhou, H. W. Jing, Q. Y. Zhang, "Failure behavior and crack evolution mechanism of a non-persistent jointed rock mass containing a circular hole", *Int. J. Rock Mech. Min. Sci.* **114** (2019), p. 101-121.
[46] Y. H. Huang, S. Q. Yang, M. R. Hall, W. L. Tian, P. F. Yin, "Experimental study on uniaxial mechanical properties and crack propagation in sandstone containing a single oval cavity", *Arch. Civ. Mech. Eng.* **18** (2018), p. 1359-1373.
[47] Y. H. Huang, S. Q. Yang, P. G. Ranjith, J. Zhao, "Strength failure behavior and crack evolution mechanism of granite containing pre-existing non- coplanar holes: experimental study and particle flow modeling", *Comput. Geotech.* **88** (2017), p. 182-198.